

**BULETINUL  
INSTITUTULUI  
POLITEHNIC  
DIN IAȘI**

**Volumul 64 (68)  
Numărul 1**

**Secția  
MATEMATICĂ  
MECANICĂ TEORETICĂ  
FIZICĂ**

**2018**

**Editura POLITEHNIUM**



**BULETINUL INSTITUTULUI POLITEHNIC DIN IAȘI**  
PUBLISHED BY  
**“GHEORGHE ASACHI” TECHNICAL UNIVERSITY OF IAȘI**  
Editorial Office: Bd. D. Mangeron 63, 700050, Iași, ROMANIA  
Tel. 40-232-278683; Fax: 40-232-211667; e-mail: buletin-ipi@tuiasi.ro

**Editorial Board**

*President:* **Dan Cașcaval**,  
*Rector* of the “Gheorghe Asachi” Technical University of Iași  
*Editor-in-Chief:* **Maria Carmen Loghin**,  
*Vice-Rector* of the “Gheorghe Asachi” Technical University of Iași  
*Honorary Editors of the Bulletin:* **Alfred Braier**,  
**Mihail Voicu**, Corresponding Member of the Romanian Academy,  
**Carmen Teodosiu**

*Editors in Chief of the* **MATHEMATICS. THEORETICAL MECHANICS.**  
**PHYSICS Section**

**Maricel Agop, Narcisa Apreutesei-Dumitriu,**  
**Daniel Condurache**

*Honorary Editors:* **Cătălin Gabriel Dumitraș**

*Associated Editor:* **Petru Edward Nica**

**Scientific Board**

**Sergiu Aizicovici**, University “Ohio”, U.S.A.  
**Constantin Băcuță**, University “Delaware”, Newark,  
Delaware, U.S.A.

**Masud Caichian**, University of Helsinki, Finland

**Adrian Cordunenu**, “Gheorghe Asachi” Technical  
University of Iași

**Constantin Corduneanu**, University of Texas,  
Arlington, USA.

**Piergiulio Corsini**, University of Udine, Italy

**Sever Dragomir**, University “Victoria”, of Melbourne,  
Australia

**Constantin Fetecău**, “Gheorghe Asachi” Technical  
University of Iași

**Cristi Foça**, University of Lille, France

**Tasawar Hayat**, University “Quaid-i-Azam” of  
Islamabad, Pakistan

**Radu Ibănescu**, “Gheorghe Asachi” Technical  
University of Iași

**Bogdan Kazmierczak**, Inst. of Fundamental Research,  
Warsaw, Poland

**Liviu Leontie**, “Al. I. Cuza” University, Iași  
**Rodica Luca-Tudorache**, “Gheorghe Asachi”  
Technical University of Iași

**Radu Miron**, “Al. I. Cuza” University of Iași  
**Iuliana Oprea**, Colorado State University, U.S.A  
**Viorel-Puiu Păun**, University “Politehnica” of  
București

**Lucia Pletea**, “Gheorghe Asachi” Technical  
University of Iași

**Irina Radinschi**, “Gheorghe Asachi” Technical  
University of Iași

**Themistocles Rassias**, University of Athens, Greece

**Behzad Djafari Rouhani**, University of Texas at El  
Paso, USA

**Cristina Stan**, University “Politehnica” of București  
**Wenchang Tan**, University “Peking” Beijing, China

**Petre P. Teodorescu**, University of București

**Anca Tureanu**, University of Helsinki, Finland

**Vitaly Volpert**, CNRS, University “Claude Bernard”,  
Lyon, France



**Secția**

**MATEMATICĂ. MECANICĂ TEORETICĂ. FIZICĂ**

S U M A R

	<u>Pag.</u>
ELENA PUIU (COSTESCU), LIVIU LEONTIE, MIHAI DUMITRAȘ, MIHAI ASANDULESA, DORIN VĂIDEANU și TUDOR- CRISTIAN PETRESCU, Comportamentul termodinamic al „lemnului lichid” (engl., rez. rom.) . . . . .	9
FRANCISCA GEORGIANA HUȘANU, MARIUS MIHAI CAZACU, GEORGIANA BULAI, SILVIU GURLUI și ELENA PETTINELLI, Măsurători de laborator pentru caracterizarea parametrilor fizici ai geomaterialelor și ai analogilor planetari (engl., rez. rom.) . . . . .	17
LIDIA-MARTA AMARANDI, FLORIN UNGA, IOANA-ELISABETA POPOVICI, PHILIPPE GOLOUB, MARIUS MIHAI CAZACU, SILVIU-OCTAVIAN GURLUI, LUC BLAREL and MARIE CHOËL, Măsurători mobile ale distribuției granulometrice și estimarea concentrațiilor de masă cu un senzor de cost redus în Lille, nordul Franței (engl., rez. rom.) . . . . .	25
VLAD GHIZDOVĂȚ, IGOR NEDELCIUC, CIPRIANA ȘTEFĂNESCU, ANDREI ZALA, MARICEL AGOP și NICOLAE DAN TESLOIANU, Ocluzia arterei coronariene explicată prin intermediul unui model fractal (engl., rez. rom.) . . . . .	37
VLAD GHIZDOVĂȚ, MIHAI MARIUS GUȚU și CIPRIANA ȘTEFĂNESCU, Coerența în structurile fractale (engl., rez. rom.) . . . . .	45
IRINEL CASIAN BOTEZ și MARICEL AGOP, Asupra unei simetrii „ascunse” a ecuațiilor lui Maxwell (engl., rez. rom.) . . . . .	59



**Section**

**MATHEMATICS. THEORETICAL MECHANICS. PHYSICS**

CONTENTS

	<u>Pp.</u>
ELENA PUIU (COSTESCU), LIVIU LEONTIE, MIHAI DUMITRAȘ, MIHAI ASANDULESA, DORIN VĂIDEANU and TUDOR- CRISTIAN PETRESCU, The Thermodynamic Behavior of “Liquid Wood” (English, Romanian summary) . . . . .	9
FRANCISCA GEORGIANA HUȘANU, MARIUS MIHAI CAZACU, GEORGIANA BULAI, SILVIU GURLUI and ELENA PETTINELLI, Laboratory Measurements for the Characterization of the Physical Parameters of Geomaterials and Planetary Analogues (English, Romanian summary) . . . . .	17
LIDIA-MARTA AMARANDI, FLORIN UNGA, IOANA-ELISABETA POPOVICI, PHILIPPE GOLOUB, MARIUS MIHAI CAZACU, SILVIU-OCTAVIAN GURLUI, LUC BLAREL and MARIE CHOËL, Investigation of Atmospheric Particulate Matter (PM) Mass Concentration Spatial Variability by Means of On-Foot Mobile Measurements in Lille, Northern France (English, Romanian summary) . . . . .	25
VLAD GHIZDOVĂȚ, IGOR NEDELCIUC, CIPRIANA ȘTEFĂNESCU, ANDREI ZALA, MARICEL AGOP and NICOLAE DAN TESLOIANU, Coronary Artery Occlusion Explained by Means of a Fractal Model (English, Romanian summary) . . . . .	37
VLAD GHIZDOVĂȚ, MIHAI MARIUS GUȚU and CIPRIANA ȘTEFĂNESCU, Coherence in Fractal Structures (English, Romanian summary) . . . . .	45
IRINEL CASIAN BOTEZ and MARICEL AGOP, On a “Hidden” Symmetry of the Maxwell’s Equations (English, Romanian summary) . . . . .	59



BULETINUL INSTITUTULUI POLITEHNIC DIN IAȘI  
Publicat de  
Universitatea Tehnică „Gheorghe Asachi” din Iași  
Volumul 64 (68), Numărul 1, 2018  
Secția  
MATEMATICĂ. MECANICĂ TEORETICĂ. FIZICĂ

## THE THERMODYNAMIC BEHAVIOR OF “LIQUID WOOD”

BY

**ELENA PUIU (COSTESCU)<sup>1\*</sup>, LIVIU LEONTIE<sup>2</sup>, MIHAI DUMITRAȘ<sup>2</sup>,  
MIHAI ASANDULESA<sup>3</sup>, DORIN VĂIDEANU<sup>2</sup> and  
TUDOR-CRISTIAN PETRESCU<sup>4</sup>**

“Gheorghe Asachi” Technical University of Iași, Romania,

<sup>1</sup>Faculty of Machine Manufacturing and Industrial Management

<sup>4</sup>Faculty of Civil Engineering and Building Services

<sup>2</sup>“Alexandru Ioan Cuza” University of Iași, Romania,

Faculty of Physics

<sup>3</sup>“Petru Poni” Institute of Macromolecular Chemistry of Iași, Romania

Received: January 9, 2018

Accepted for publication: January 25, 2018

**Abstract.** Being a material similar to a “thermoplastic”, it is essential to establish the thermodynamic performance of “liquid wood” and its thermal properties. It is intended to study the comportment of “liquid wood” in the heating-cooling process. The study of thermodynamic behavior it was carried out for different ranges of temperature cycles of heating and cooling. These temperature intervals have included negative temperatures up to  $-400^{\circ}\text{C}$  and high temperatures up to  $800^{\circ}\text{C}$ . Also, the determinations were made regarding thermal degradation of the “liquid wood”, in the tow presentation forms: Arboform and Arboblend. Considering that it the electrical properties of the “liquid wood” were previously studied, it was intended to see how these properties change with the temperature variation. The results are prone to encourage further research, thermodynamic properties of the “liquid wood” shows that they are suitable for use in many industries successfully replacing

---

\*Corresponding author; *e-mail*: naturaone@gmail.com

other traditional materials (mainly, the plastics materials) that are polluting, having a very low rate of biodegradability.

**Keywords:** weight loss; crystalline; point of inflection; phase transformations; aggregation state.

## 1. Introduction

In recent times, the need of so-called “green” materials for various engineering and product applications has increased considerably, in lieu of the adjustments of global environmental statutes and law bills. These aim to impose a cutback on the CO<sub>2</sub> emissions. The gradual exhaustion of raw resources (petroleum, natural gas) has led to much research, with the purpose of evaluating the feasibility of utilizing “green” composite materials. In support of this research, the Fraunhofer Institute, working closely with Helmut Nägele and Jürgen Pfitzer, has created the products known as Arboform and Arbofill following 13 years of effort. The abovementioned products are ordinarily known as “liquid wood”, by virtue of being amorphous at regular temperatures. They present properties similar to plastics, however they are sourced from sustainable resources and are ecological (Rognoli *et al.*, 2010).

## 2. Technology and Experimental Plan

The trials concerning thermodynamic behavior were carried out using a thermal analyzer F1 Jupiter, Netzsch STA 449, with concurrent registration of TG data (Thermal Gravimetric Analysis, in the mass of the specimen is assessed through temperature fluctuation) and DTA (Differential Thermal Analysis, where it is evaluated the temperature variation among the sample and the source temperature dependent). In order to carry out the data evaluation, Proteus 6.0 software has been utilized (Höhne *et al.*, 2013).

Samples analyzed consisted of Arboform and Arboblend grains, with the mass of approximately 40 mg. The description of the experimental environment is as follows: calefaction pace of 10 K/min, alumina-made melting pots - with confinement agent from the extraneous environment consisting of a stream of N<sub>2</sub> - with the volumetric discharge rate  $Q_v = 40$  mL/min.

Non-isothermal investigations were accomplished on a Netzsch STA 449 F1 Jupiter thermal analyzer, employing concurrent registration of TG and DTA data. Once again, Proteus 6.0 software was put to use for data assessment.

The specimens put forward to analysis were constituted of granular Arboform and Arboblend, with a sample mass of roughly 40 mg. Experimental parameters were: calefaction pace of 10 K/min, alumina-made melting pots, under a steady N<sub>2</sub> stream of 40 mL/min. The procedures involving heating and cooling were performed under a primary reference temperature of  $t_0 = 200^\circ\text{C}$ .

Regarding the change of electrical characteristics of “liquid wood” following a term of 365 days and its temperature-dependent fluctuation, the electrical conductivity and relative permittivity were evaluated, as well as the difference on two phases, in connection with the temperature.

The dielectric determinations have been executed at room temperature, with the help of a Novocontrol apparatus (Broadband dielectric spectrometer Concept 40, GmbH Germany), using the frequency spectrum of  $1 \div 10^6$  Hz, setting up the specimens of homogenous amidst two copper-plated round electrodes, through which an electric current rated at 1V passed (Musteață *et al.*, 2014).

Subsequent to the results achieved to certify the assumptions, analyzes and determinations were made. XRD crystal structure determination performed by means of X-ray specimens in fine grain form. The operating procedure is utilizing X-rays, length  $\lambda = 1.54182 \text{ \AA}$ , to retrieve an anticathode of Cu Ka.

Through the accomplishment of these analyzes it was attempted to detect if any parallels can be drawn among the structure and the thermal experiments and to ascertain the elements in the indicated materials, which are essential in establishing the thermodynamic performance of the material. In order to portray this, the results were introduced in OriginPro 9 software, which allows plotting graphs, results interpretation and facilitates the drawing of conclusions. Concerning the results obtained, which highlight the thermal properties for the three materials, the subsequent graphs were drawn (Figs. 1 and 2).

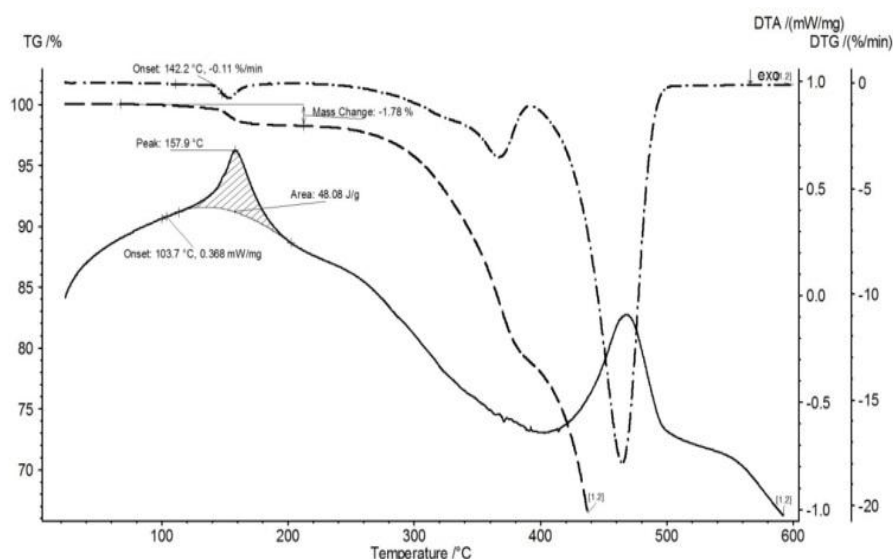


Fig. 1 – Heating curve graph for arboblend sample.

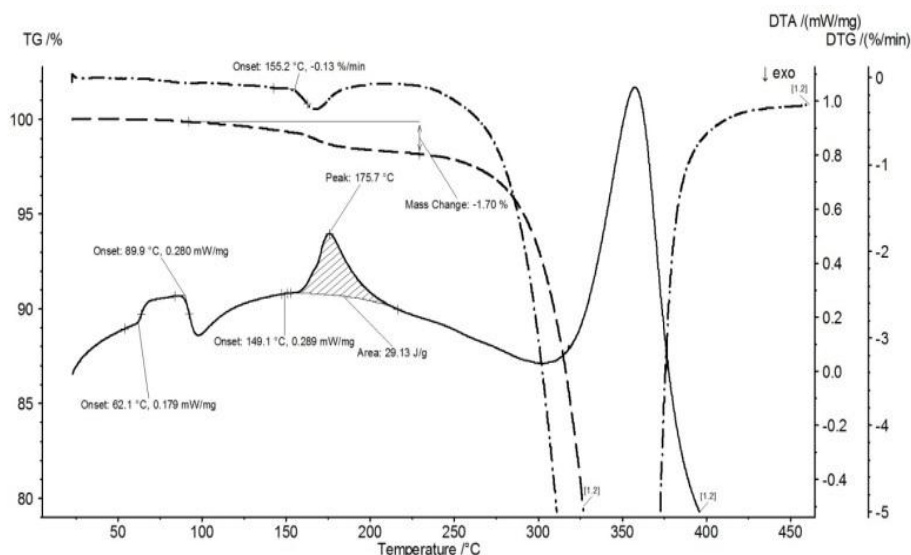


Fig. 2 – Heating curve graph for arboform sample.

Following the investigation of the three graphs several important aspects may be noticed: the melting point of arboform begins at about  $t = 103.7^{\circ}\text{C}$ , at  $t = 142.2^{\circ}\text{C}$ , temperature the entire mass of material is almost melted, only a small amount of 0.11% remains unmelted, at temperature  $t = 157.9^{\circ}\text{C}$  the entire mass of the material is melted, it can be seen that at  $t = 142.2^{\circ}\text{C}$  the material begins to lose mass (1.78%) until it melts completely. Continued warming is observed as the material gradually loses mass, culminating at temperatures above  $400^{\circ}\text{C}$  which is seen a steep drop from the table, and around  $460^{\circ}\text{C}$  a second phase transformation occurs, that is most likely a vaporization. Same phase transition for Arboform is observed, with a second order glass transition material showing a crystalline phase. The melting temperature is higher than in the case of the other two materials. In the process of melting arboform loses mass (1.7%).

Resting on these remarks and attempting to seek out probable explanations for the thermodynamic performance of the three materials, a series of experiments have been conducted, analyzing the X-ray diffraction (XRD) and spectral infrared (FTIR).

Following XRD analyzes, a series of charts were obtained that endorse the presence of a second type of transformations, analogous to a vitreous shift from a crystalline state to an amorphous one. It was in these states of the two materials that phase shifts of second type have been spotted (Fig. 3a, b).

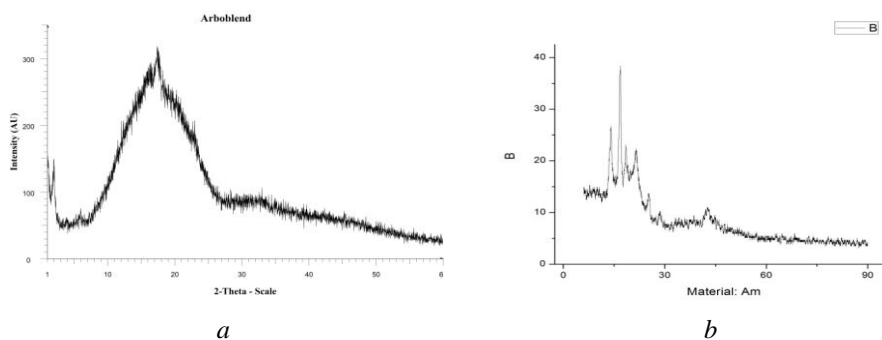


Fig. 3 – a) XRD arboblend; b) XRD arboform.

Arboblend shows no crystalline state (Fig. 3a) while Arboform shows crystalline state (Fig. 3b).

Following XRD analyzes, a series of charts were obtained that uphold the presence of a second type of transformations, analogous to a vitreous shift from a crystalline state to an amorphous one. It was in these states of the two materials that phase shifts of second type have been spotted (Fig. 3a, b) (Nägele *et al.*, 2005).

Lignin behaves as a forming agent for the biodegradable composite and promotes crystallization. The extent of the lignin substance (amorphous in itself) takes part in the polymer crystallization process (Madden *et al.*, 1971).

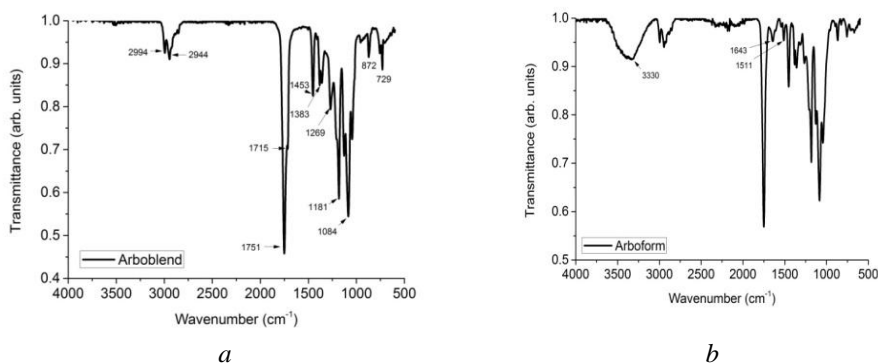


Fig. 4 – a) Grafic FTIR arboblend; b) Grafic FTIR arboform.

The samples don't seem to contain polymers with aminic and/or amidic functions. Arboblend it looks like it doesn't contain OH functions and only very small or no aromatic functions; it is possible however that the OH functions were crosslinked during manufacturing (the estheric and etheric signal is stronger than in Arboform, plus the probable supplementary estheric signal is

from  $1269\text{ cm}^{-1}$ ). Arboform has spectral characteristics relatively close to Arboblend (possibly a high percentage of polihydroxycanoates and other added polyesters/polyethers), the notable exceptions being given by the presence of OH functions and a signal possibly given off by aromatic rings from lignin derivatives (Puiu Costescu *et al.*, 2017).

The dielectric characteristics of materials - illustrated by the dielectric constant,  $\epsilon'$ , the dielectric loss,  $\epsilon''$  AC conductivity,  $\sigma$  etc. - hinge on their chemical architecture. The dielectric feedback has been recorded in the 1 Hz – 1 MHz frequency spectrum and in the 20 – 100°C temperature interval.

Fig. 5 displays the development of the dielectric constant with regard to frequency, for analyzed samples.  $\epsilon'$  diminishes steadily along with the frequencies, because of the capability of dipolar units to adjust themselves in the path of the exterior field. As such, at small frequencies, the dipoles have sufficient time to trail the alternate electric field but, as frequency escalates, the dipoles require more time than the applied field, thus the magnitude of  $\epsilon'$  is reduced.

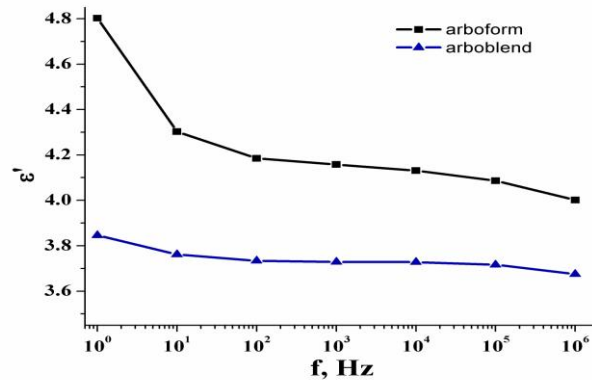


Fig. 5 – Comparative evolution of the dielectric constant function of frequency ( $T = 30^\circ\text{C}$ ).

AC conductivity was obtained from the dielectric loss with the help of the following formula:

$$\sigma_{AC} = \epsilon_0 \omega \epsilon'' \quad (1)$$

where  $\epsilon_0$  is the permittivity of free space,  $\omega$  is the angular velocity and  $\epsilon''$  is the dielectric loss.

AC conductivity grows together with frequency in an obverse way than the dielectric constant (Fig. 6). At a frequency of 1 Hz, the values of conductivity are:  $4.2 \times 10^{-13}$  S/cm for Arboform,  $5.1 \times 10^{-13}$  S/cm for Arboblend and  $1.2 \times 10^{-13}$  S/cm for Arboblend sample. The values are specific to insulator materials.

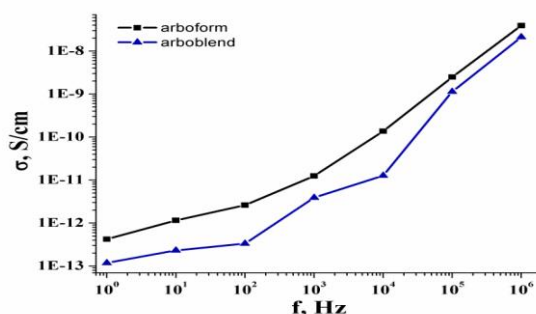


Fig. 6 – AC conductivity change in concert with frequency at 30°C.

Fig. 7 shows the temperature dependencies of conductivity for all analyzed samples. Accordingly, one can observe the possible thermal transitions at 25°C, 70°C and around 90°C.

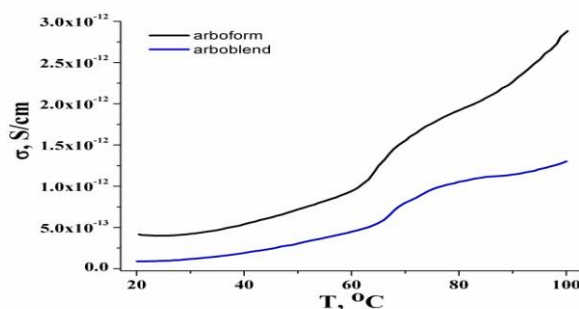


Fig. 7 – Temperature dependences of AC conductivity.

### 3. Conclusions

The studied materials behave during the heating process as amorphous solids. Arboform have in their composition a substance which can be found in a crystallized form in the temperature interval [65°C – 90°C]. Arboblend exhibits a loss of mass until it reaches its liquid state. A possible cause may be the evaporation of one of its constituents. It might be a substance which acts as a binder for the material.

During the melting process, Arboform loses mass, the explanation being similar to the one for Arboblend. The melting temperature of Arboform is bigger than in the case of Arboblend; this means that this material is more stable, from a temperature point of view. Arboform evaporates at a smaller temperature than Arboblend. This aspect might induce the idea that this material has a higher degradability than Arboblend.

The lignin that can be found in the composition of the three materials has undergone transformations and is not to be found anymore in the molecular shape present in wooden fibers.

## REFERENCES

- Höhne G., Hemminger W.F., Flammersheim H.-J., *Differential Scanning Calorimetry in: An Introduction for Practitioners*, Springer (2013).
- Madden J.P., Baker G.K., Smith C.H., *Study of Polyether-Polyol- and Polyesterpolyol-Based Rigid Urethane Foam Systems*, Technical Report Made for United States Department of Energy and Paper Submitted to 162nd National Meeting, Washington, DC: American Chemical Society (1971).
- Nägele H., Pfitzer J., Lehnberger C., Landeck H., *Renewable Resources for Use in Printed Circuit Boards*, Circuit World, ProQuest Central, **31**, 2, 26 (2005).
- Puiu Costescu E., Văideanu D., Băcăiță S., Agop M., *Thermal and Electrical Behaviors of the Arbofill Liquid Wood*, Internațional Journal of Modern Manufacturing Technologies, **4**, 1, 79-83 (2017).
- Rognoli V., Salvia G., Manenti S., *Un'identità per i biopolimeri: il caso del legno lichido*, 77-83 (2010).
- Musteață V.E., Grigoraș V.C., Bărboiu V., *Correlation of Dielectric and Calorimetric Characteristics for an Amorphous Donor-Acceptor Copolymer*, Revue Roumanie de Chimie, **59**, 6-7, 503-509 (2014).

## COMPORTAMENTUL TERMODINAMIC AL „LEMNULUI LICHID”

(Rezumat)

Fiind un material asemănător unui „termoplastic” este foarte important de determinat comportamentul termodinamic al „lemnului lichid” cât și proprietățile termice și electrice ale acestuia. Ne-am propus să studiem comportamentul lemnului lichid în cadrul procesului de încălzire-răcire. Studiul comportamentului termodinamic s-a efectuat pentru diverse intervale de temperatură a ciclurilor de încălzire și răcire. Aceste intervale de temperatură au cuprins și temperaturi negative de până la  $-40^{\circ}\text{C}$  și temperaturi ridicate de până la  $800^{\circ}\text{C}$ . S-au efectuat determinări și în ce privește degradarea termică a „lemnului lichid” sub două forme de prezentare: arboform și arboblend. Ținând cont că anterior am efectuat studii asupra proprietăților electrice ale „lemnului lichid” am căutat să vedem cum se modifică aceste proprietăți la variația temperaturii. Rezultatele obținute sunt de natură să încurajeze continuarea cercetărilor, proprietățile termodinamice ale „lemnului lichid” îl recomandă spre a fi utilizat în multe domenii de activitate, înlocuind cu succes alte materiale clasice, dar care sunt poluante, având o biodegradabilitate foarte scăzută, care se produce într-un interval de timp de câteva sute de ani.

BULETINUL INSTITUTULUI POLITEHNIC DIN IAȘI  
Publicat de  
Universitatea Tehnică „Gheorghe Asachi” din Iași  
Volumul 64 (68), Numărul 1, 2018  
Secția  
MATEMATICĂ. MECANICĂ TEORETICĂ. FIZICĂ

**LABORATORY MEASUREMENTS FOR THE  
CHARACTERIZATION OF THE PHYSICAL PARAMETERS OF  
GEOMATERIALS AND PLANETARY ANALOGUES**

BY

**FRANCISCA GEORGIANA HUȘANU<sup>1</sup>, MARIUS MIHAI CAZACU<sup>1,2,\*</sup>,  
GEORGIANA BULAI<sup>3</sup>, SILVIU GURLUI<sup>1</sup> and ELENA PETTINELLI<sup>4</sup>**

“Alexandru Ioan Cuza” University of Iași, Romania,

<sup>1</sup>Atmosphere Optics, Spectroscopy and Lasers Laboratory (LOA-SL), Faculty of Physics

<sup>3</sup>Integrated Center for Studies in Environmental Science for North-East Region (CERNESIM)

<sup>2</sup>“Gheorghe Asachi” Technical University of Iași, Romania,

Department of Physics

<sup>4</sup>Roma Tre University, Italy,

Laboratory of Earth and Planetary Applied Physics

Received: January 29, 2018

Accepted for publication: February 27, 2018

**Abstract.** Ice can be found in our Solar System, from the presence of ice water on Mars at the poles, water vapor in the atmosphere to ice-covered moons and icy crust composed of H<sub>2</sub>O found on the moons of Jupiter and Saturn. Sea ice is frozen sea water that floats on the ocean surface. This paper presents the results of an experimental work concerning the electric properties of sea ice samples. The objectives were to determine the electric properties of the sea ice samples and to investigate how these properties vary in function of temperature and frequency. The sea ice samples were analyzed using a vector network analyzer connected to a three-wire open transmission line immersed in the saline solution. For sea ice sample a large variation of the real part of permittivity with temperature around the eutectic point was observed.

**Keywords:** sea ice; transmission line; permittivity; conductivity.

---

\*Corresponding author; *e-mail*: marius.cazacu@tuiasi.ro

## 1. Introduction

Sea ice is a thin and solid layer that forms by the freezing of surface seawater and is characterized by a multiphase structure that includes ice crystals as well as gas, liquid brines, solid salts and other impurities (Thomas and Diekmann, 2009). At low temperatures, sea ice forms on the ocean's surface, starting as a thin sheet of crystals that grow into a salty ice. Salt particles called brines are trapped in the ice crystals as they freeze. When no water turbulences are present, their growth is regular and a uniform columnar ice type is formed with the c-axis of the crystals aligned in the horizontal plane. In such a structure, brine inclusions can potentially migrate downwards along vertically oriented channels whose shape is governed by the temperature (Reid *et al.*, 2006). Sea ice has a bright surface that reflects sunlight back into space. Because the areas covered by sea ice absorb little solar energy, the temperatures in the polar regions are relatively cool.

If the physical properties of the fresh-water ice, are well known, the sea ice is a relatively complex substance and its properties are still under study. The transformation to a completely solid mixture of pure ice and solid salts is attained only at very low temperatures, so extreme that they are rarely encountered in nature. The physical properties of sea ice depend strongly on salinity, temperature and age (Schwerdtfeger, 1963).

The salinity of sea ice is governed by both age and location. For example, because of its rapid formation Antarctic first year sea ice contains more brine trapped in its granular structure, and remains quite saline with time (Mattei *et al.*, 2017).

Global warming still affects sea ice formation because when the increasingly warming temperatures melt sea ice, less bright surfaces are available to reflect sunlight back into space. The Solar energy is absorbed at the surface, and temperatures increase further (Weeks, 2010).

The study of Arctic sea ice has recently gathered importance for both climate change monitoring (Vinnikov *et al.*, 1999; Vihma, 2014) and possible trans-Arctic trade shipping along the Northwest Passage (Ho, 2010).

In the present study, we focus on the electric and magnetic properties of the sea ice samples and how these properties vary in function of temperature and frequency.

## 2. Experimental Details

The sea ice sample was prepared by dissolving approximately 55.55 grams of sodium chloride in 1.8 liters of water. Estimation of electromagnetic properties was done according to temperature (from liquid to solid state) using a vector network analyzer connected to a tri-wire open transmission line immersed in the saline solution. To carry out measurements as a function of

temperature, the sample was inserted into a climatic chamber where a 200 K temperature is reached.

The experimental device presented in Fig. 1 is divided into three parts: the climatic chamber where the sea ice sample is formed, the network analyzer vector where the collected data from the sample are recorded and the computer.

The already prepared saline solution of 35 grams/liter was introduced in the climatic chamber at a temperature of  $-75^{\circ}\text{C}$ .

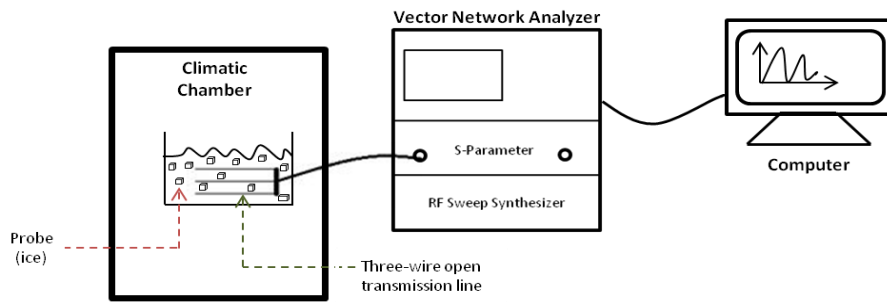


Fig. 1 – Scheme of the experimental setup.

To measure the electrical properties ( $\epsilon'_r, \epsilon'' = \sigma/\omega\epsilon_0$ ) of a non-magnetic medium ( $\mu_r = 1$ ) we used a transmission line that is filled with the material to be analyzed and terminates with an infinite impedance (transmission line open at its termination). Because  $Z_{L \rightarrow \infty}$  the input admittance  $Y_{in}$  of the probe is described by Eq. (1):

$$Y_{in} = \frac{1}{Z_{cable}} \frac{1-S_{11}}{1+S_{11}} = iY_c \tan(kl) = iY_{c0} \sqrt{\epsilon'_r - i\sigma/\omega\epsilon_0} \tan\left(\frac{\omega}{c} \sqrt{\epsilon'_r - i\sigma/\omega\epsilon_0} l\right) \quad (1)$$

where  $Z_{cable} = 50 \Omega$  is the cable impedance,  $Y_c$  is the characteristic admittance of the line in the absence of material,  $c$  is the speed of light in vacuum and  $l$  is the length of the line.

At low frequency ( $kl = \frac{\omega}{c} \sqrt{\epsilon'_r - i\sigma/\omega\epsilon_0} l \rightarrow 0$ ), the input admittance can be approximated as follows, Eq. (2):

$$Y_{in} \cong iY_{c0} \frac{\omega}{c} l \left( \epsilon'_r - i \frac{\sigma}{\omega\epsilon_0} \right) = i\omega C_{lf} \left( \epsilon'_r - i \frac{\sigma}{\omega\epsilon_0} \right), \omega \rightarrow 0 \quad (2)$$

where  $C_{lf} = Y_{c0} l/c$  is the low-frequency line capacity that can be estimated by calibration measurements.

Electrical conductivity was calculated from the real part of the admittance which depends on the scattering parameter  $S_{11}$ , Eq. (3).

$$\sigma = \frac{\varepsilon_0}{C_{lf}} \operatorname{Re}\{Y_{in}\} = \frac{\varepsilon_0}{Z_{cable} C_{lf}} \operatorname{Re}\left\{\frac{1-S_{11}}{1+S_{11}}\right\} \quad (3)$$

The real part of permittivity is given by, Eq. (4):

$$\varepsilon_r' = \frac{1}{\omega C_{lf}} \operatorname{Im}\{Y_{in}\} = \frac{1}{Z_{cable} \omega C_{lf}} \operatorname{Im}\left\{\frac{1-S_{11}}{1+S_{11}}\right\} \quad (4)$$

At high frequencies ( $\vartheta \gg \frac{\sigma}{2\pi\varepsilon_0\varepsilon_r}$ ) where  $\frac{\omega}{c} \operatorname{Re}\{\sqrt{\varepsilon_r}\}l = \pi/2$ , the imaginary part of admittance tends to diverge and the real part has the maximum.

This allows the estimation of the real part and the imaginary part of the permittivity at frequencies  $\vartheta_m$  for which  $\frac{2\pi}{c} \vartheta_m \sqrt{\varepsilon_r} l \cong (2m-1)\pi/2$ :

$$\begin{aligned} \varepsilon_r'(\vartheta_m) &= \left(\frac{c}{2\pi\vartheta_m l}\right)^2 \left\{ \left[\frac{\pi}{2}(2m+1)\right]^2 - \left[\operatorname{arccoth}\left(\frac{1}{2m+1} \frac{4\vartheta_m l}{c} \operatorname{Re}\left\{\frac{Y_{in}(\vartheta_m)}{Y_{c0}}\right\}\right)\right]^2 \right\} \\ &\cong \left[(2m+1) \frac{c}{4\vartheta_m l}\right]^2 \end{aligned} \quad (5)$$

$$\varepsilon_r''(2m+1)\pi \left(\frac{c}{2\pi\vartheta_m l}\right)^2 \operatorname{arccoth}\left(\frac{1}{2m+1} \frac{4\vartheta_m l}{c} \operatorname{Re}\left\{\frac{Y_{in}(\vartheta_m)}{Y_{c0}}\right\}\right) \quad (6)$$

$$\sigma(\vartheta_m) = \omega_m \varepsilon_0 \varepsilon_r''(\vartheta_m) \quad (7)$$

To study the electromagnetic properties of the sample, it was necessary to estimate the geometric factors of the transmission line ( $C_{lf}$ ,  $Y_{c0}$ ,  $e$ ,  $l$ ); Knowing these parameters, we were able to evaluate the real part of permittivity and conductivity at low frequency using Eqs. (3) and (4) and the real part of permittivity and conductivity at high frequency using Eqs. (5) and (7).

The low-frequency capacity was estimated from the measurements done with the vector network analyzer on a sample of water and the conductivity measurement on the same sample made with the electrical conductivity meter by applying Eq. (3). Using the same data, the line length  $l$  could be calculated using Eq. (5) in its approximate form considering that the real part of the permittivity is  $\varepsilon_r' = 87.9 - 0.4T + 9.5 \times 10^{-4} T^2 - 1.3 \times 10^{-6} T^3$  ( $T$  is the temperature in Celsius degrees).

### 3. Results and Discussion

To obtain the dielectric properties of the sample, we plotted both the real part of the permittivity (Fig. 2) and the conductivity (Fig. 3) with

temperature. The real part of the permittivity for 4 different frequencies was recorded. From these graphs one can observe that the temperature at which the sample begins to melt is 252 K. Below this temperature, the water is frozen uniformly, and above this temperature liquid areas (brines zones) begin to appear inside the ice. Under these conditions, the instrument can measure the real part of permittivity only at low frequencies. Above the eutectic temperature, the high frequency estimate of  $\epsilon'_r$  and  $\sigma$  can not be performed because the medium is too attenuating.

As a function of temperature, a large variation of the real part around the eutectic temperature is observed. Fig. 2 also shows that the real part of permittivity is higher for the lowest frequency. Electrical properties are very sensitive to the physical state of the sample.

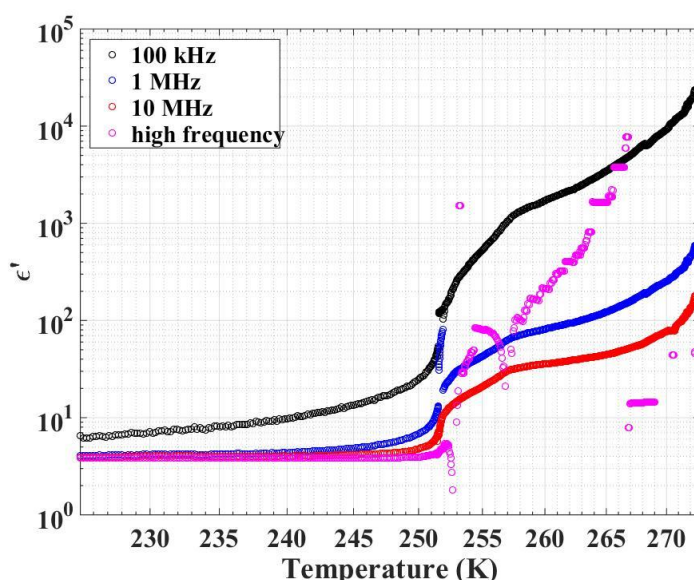


Fig. 2 – The real part of the permittivity as a function of temperature.

A greater variation of the conductivity versus the variation of the real part of the permittivity is observed around the eutectic temperature. This is due to the fact that conductivity is a physical parameter that generally varies greatly. When the temperature is high, the conductivity is due to the conductivity of the brines. Similar results have been obtained by (Moore *et al.*, 1994). In this study the conductivity values varied between  $10^3$  to  $10^4$   $\mu\text{S/m}$ , as the frequency was changed from several kHz up to a few MHz on both synthetic and natural sea ice grown under different conditions.

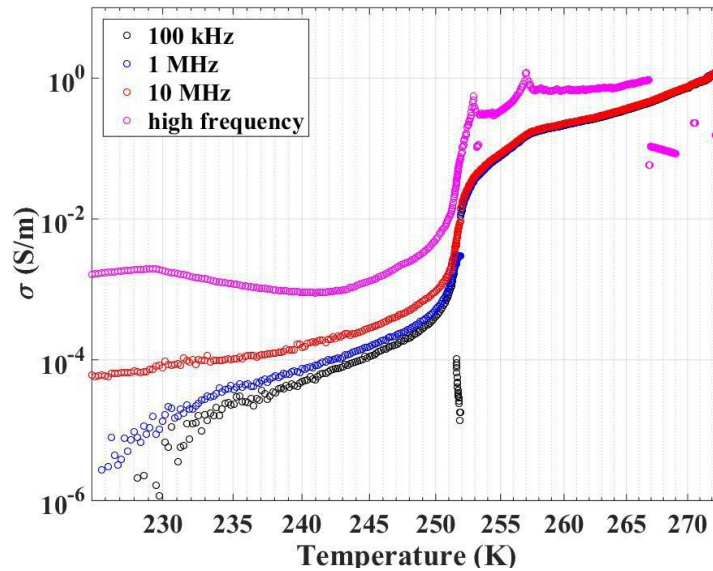


Fig. 3 – Conductivity as a function of temperature.

In liquid phase, the conductivity of the sample does not depend on the frequency. When the sample passes in a solid state, we observe a small dependence with the frequency as a response of charges produced by the self-dissociation of  $H_2O$  molecules (Artemov and Volkov, 2014).

The experimental results obtained by these experiments have permitted a better definition of the dielectric behaviour of sea ice.

### 3. Conclusions

The main objectives of this work were to determine the electromagnetic properties (permittivity and conductivity) of sea ice sample and to investigate how these properties vary with temperature and frequency.

For sea ice sample we observed a large variation of the real part of permittivity as a function of the temperature around the eutectic point. We also observed that the real part of permittivity increases when decreasing the frequency. The conductivity measurements showed a greater variation with temperature than the ones of the real part of the permittivity at 252 K.

The measurement of dielectric properties of ice salted water reflects the effects of environmental parameters and conditions that operate on geomaterials.

**Acknowledgements.** This work was financially supported by the Romanian Space Agency (ROSA) within Space Technology and Advanced Research (STAR) Program, Project number 162/20.07.2017 and 169/20.07.2017.

## REFERENCES

- Artemov V.G., Volkov A.A., *Water and Ice Dielectric Spectra Scaling at 0°C*, *Ferroelectrics*, **466**, 158-165 (2014).
- Ho J., *The Implications of Arctic Sea Ice Decline on Shipping*, *Mar. Policy*, **34**, 3, 713-715, May 2010.
- Mattei E., Di Paolo F., Cosciotti B., Lauro S.E., Pettinelli E., *Young Sea Ice Electric Properties Estimation under Non-Optimal Condition*, *Advanced Ground Penetrating Radar (IWAGPR)*, July 2017, 10.1109/IWAGPR.2017.7996110.
- Moore J.C., Reid A.P., Kipfstuhl J., *Microstructure and Electrical Properties of Marine Ice and its Relationship to Meteoric Ice and Sea Ice*, *J. Geophys. Res. Oceans*, **99**, C3, 5171-5180, March 1994.
- Reid J.E., Pfaffling A., Worby A.P., Bishop J.R., *In situ Measurements of the Direct-Current Conductivity of Antarctic Sea Ice: Implications for Airborne Electromagnetic Sounding of Sea-Ice Thickness*, *Ann. Glaciol.*, **44**, 217-223, November 2006.
- Schwerdtfeger P., *The Thermal Properties of Sea Ice*, *Journal of Glaciology*, **4**, 789-807 (1963).
- Thomas D.N., Dieckmann G.S., *Sea Ice*. Hoboken, NJ: John Wiley & Sons, 2009.
- Vinnikov K.Y., Robock A., Stouffer R.J., Walsh J.E., Parkinson C.L., Cavalieri D.J., Mitchell J.F.B., Garrett D., Zakharov V.F., *Global Warming and Northern Hemisphere Sea Ice Extent*, *Science*, **286**, 5446, 1934-1937, December 1999.
- Vihma T., *Effects of Arctic Sea Ice Decline on Weather and Climate: A Review*, *Surv. Geophys.*, **35**, 5, 1175-1214, March 2014.
- Weeks W.F., *On Sea Ice*, University of Alaska Press (2010).

MĂSURĂTORI DE LABORATOR PENTRU  
CARACTERIZAREA PARAMETRILOR FIZICI AI GEOMATERIALELOR  
ȘI AI ANALOGILOR PLANETARI

(Rezumat)

Sunt raportate rezultatele unui studiu experimental privind proprietățile electrice și magnetice ale gheții marine. Scopul acestui studiu a fost investigarea proprietăților electromagnetice ale probelor de gheață marină și modul în care aceste proprietăți variază în funcție de temperatură și frecvență. Un alt obiectiv al acestui studiu a fost acela de a observa procesele care se produc atunci când apa marină trece din stare lichidă la stare solidă și înțelegerea modului în care funcționează analizorul de rețea și camera climatică. O discuție despre variația conductivității a fost făcută prin comparație cu rezultate anterioare ale altui grup de cercetare.



BULETINUL INSTITUTULUI POLITEHNIC DIN IAȘI  
Publicat de  
Universitatea Tehnică „Gheorghe Asachi” din Iași  
Volumul 64 (68), Numărul 1, 2018  
Secția  
MATEMATICĂ. MECANICĂ TEORETICĂ. FIZICĂ

**INVESTIGATION OF ATMOSPHERIC PARTICULATE  
MATTER (PM) MASS CONCENTRATION SPATIAL  
VARIABILITY BY MEANS OF ON-FOOT MOBILE  
MEASUREMENTS IN LILLE, NORTHERN FRANCE**

BY

**LIDIA-MARTA AMARANDI<sup>1</sup>, FLORIN UNGA<sup>2</sup>, IOANA-ELISABETA  
POPOVICI<sup>2,3</sup>, PHILIPPE GOLOUB<sup>2</sup>, MARIUS MIHAI CAZACU<sup>1,4,\*</sup>,  
SILVIU-OCTAVIAN GURLUI<sup>1</sup>, LUC BLAREL<sup>2</sup> and MARIE CHOËL<sup>5</sup>**

<sup>1</sup>“Alexandru Ioan Cuza” University of Iași, Romania,  
Atmosphere Optics, Spectroscopy and Lasers Laboratory (LOA-SL), Faculty of Physics  
University of Lille, France,

<sup>2</sup>CNRS, UMR8518 – LOA – Laboratoire d’Optique Atmosphérique

<sup>5</sup>CNRS, UMR8516 – LASIR – Laboratoire de Spectrochimie Infrarouge et Raman

<sup>3</sup>CIMEL Electronique, Paris, France

<sup>4</sup>“Gheorghe Asachi” Technical University of Iași, Romania,  
Department of Physics

Received: February 26, 2018

Accepted for publication: March 23, 2018

**Abstract.** Air-quality and pollution levels in urban agglomerations are generally assessed by monitoring stations set up in fixed locations. However, the particulate matter (PM<sub>10, 2.5, 1</sub>) mass concentrations at surface level, which are hazardous for environment and human health, can be highly variable in space and time even at a local scale. Thus, there is a need for assessing the spatial distribution of the particulate matter loadings at fine spatial scale. For this, we performed on-road mobile measurements of particle size distributions with a low-cost sensor, Alphasense OPC-N2, in order to estimate the PM<sub>10, 2.5, 1</sub> mass concentration. The measurements were performed in the urban regions of Lille metropolis, in northern France. In this work, we evidence the gradients of

---

\*Corresponding author; *e-mail*: marius.cazacu@tuiasi.ro

pollution levels between less and more densely populated areas. In our study, we found an increased level of  $PM_x$  concentrations higher than  $40 \mu\text{g}/\text{m}^3$  near the commercial centers, as well in the city center, whereas regions with less traffic and more rural areas (Villeneuve d'Ascq) are less polluted.

**Keywords:** PM; urban measurements; on-road measurements; low-cost sensors; pollution gradients.

## 1. Introduction

Aerosols are a ubiquitous and variable component in the Earth's atmosphere (Mann *et al.*, 2014). Their spatio-temporal distribution is highly variable (Kinne *et al.*, 2006; Yu *et al.*, 2012). The aerosol microphysical properties, such as size, shape, mixing state and also chemical composition strongly depend on their emission sources (de Meij *et al.*, 2012; Fuzzi *et al.*, 2015) and on the transformation processes they suffer during their transport from the source. Atmospheric processes occurring during the aerosol lifetime, *e.g.* heterogeneous reactions at the surface of each particle, hygroscopic growth due to the water uptake and physicochemical aging will undergo important changes on their microphysical and micro-chemical characteristics, but also on their optical properties (Johnson *et al.*, 2005; Müller *et al.*, 2017; Nessler *et al.*, 2005; Niemi *et al.*, 2006). Such properties and quantitative assessment of the ambient particulate matter loadings are important for air-quality studies and evaluation of their impact on human health (Fuzzi *et al.*, 2015; Ignotti *et al.*, 2010; Pöschl, 2005).

In urban areas, the air quality and pollution levels are assessed by stationary monitoring stations, *e.g.* (Ielpo *et al.*, 2014). As previously mentioned, the particulate matter of various sizes, namely  $PM_{10}$ ,  $PM_{2.5}$ , and  $PM_1$ , which represent the mass concentration of particles with diameter sizes no larger than  $10 \mu\text{m}$ ,  $2.5 \mu\text{m}$  and  $1 \mu\text{m}$ , respectively, presents a high variability in space and time. The fixed air-quality stations can be located at various geographical distances, from couple of kilometers to hundreds of kilometers (see the World Quality Index website for a detailed map of the global locations of air quality monitoring stations: <http://aqicn.org/>). But, there is no information on the PM concentration levels at fine spatial scale. Chemistry transport models (Crippa *et al.*, 2016) and satellites measurements and retrieved products can provide global maps of aerosol loadings and their physical, chemical and optical properties (Mallet *et al.*, 2016), but their spatial scale is limited and varies from  $1 \text{ km}^2$  to a couple of  $\text{km}^2$ . Thus, there is a need to study this variability of the ambient PM concentrations at fine scale.

In order to achieve such fine spatial scale studies, we perform on-road mobile measurements using a low-cost optical particles counter to measure particles size distribution and assess PM number and mass concentrations. This

paper presents a simple methodology to conduct mobile measurements at small scale and results obtained from a field campaign conducted in the urban agglomeration of Lille, northern France. Taking into consideration the impact of air pollution on our lives, we evaluate the variability of PM mass concentration in various environments, *e.g.* more and less densely populated areas such as green spaces and the vicinity of the commercial centers.

## 2. Instruments and Methodology

The instrument used for measurements is an Optical Particle Counter (OPC-N2), from Alphasense (<http://www.alphasense.com/>), that measures the light (from a diode laser source) scattered by a particle from the sampled environmental air stream. Based on Mie theory (Van de Hulst, 1981), the instrument classifies the particles by their optical diameter and determines their number concentration.  $PM_{10}$ ,  $PM_{2.5}$  and  $PM_{10}$  mass concentrations are then calculated from the particle size spectra and the number concentration data. To calculate the mass concentration, it is generally considered that the particles density is  $1.65 \text{ g/cm}^3$  and the refractive index, RI, (a complex number with its imaginary part related to particles' absorption), is  $1.5+i0$  (Alphasense User Manual OPC-N2 Optical Particle Counter, 2015). OPC-N2 uses an elliptical mirror to create a sensing volume and a dual-element photo detector to measure the scattered light. The measurements are idealized by ignoring the absorption coefficient, which is usually in the range of 0.01 to 0.1 (Lieberman, 1992). The instrument can measure particles in the size range between  $0.38 \text{ }\mu\text{m}$  and  $17 \text{ }\mu\text{m}$  diameter and the detection limits are from  $0.01 \text{ }\mu\text{g/m}^3$  to  $1500 \text{ mg/m}^3$ . The particle size is recorded in 16 size bins in a sampling interval from 1 to 10 seconds, with a maximum of 10000 particles/second (Alphasense User Manual OPC-N2 Optical Particle Counter, 2015). The sampling interval chosen in this study was 60 seconds.

Fig. 1 illustrates the setup for the mobile measurements. It consists of the optical particle counter (Fig. 1a) installed in the lateral pockets of the backpack, a GPS (Fig. 1b) and a laptop inside the backpack (Fig. 1c). A second OPC was installed, in case of technical problems with the first one. In order to visualize the recorded data during on-road measurements, a commercial USB Internet modem was used. This can assure the possibility of the user to access the real-time measurements by remote controlling software (Crilley *et al.*, 2018; Bezantakos *et al.*, 2017).

The GPS used for the measurements is a BU-353 model, water resistant and having an active patch antenna for a better accuracy. The GPS is connected to the laptop via an USB cable and there is no need of batteries or other power source (US GlobalSat Corporate, 2014).

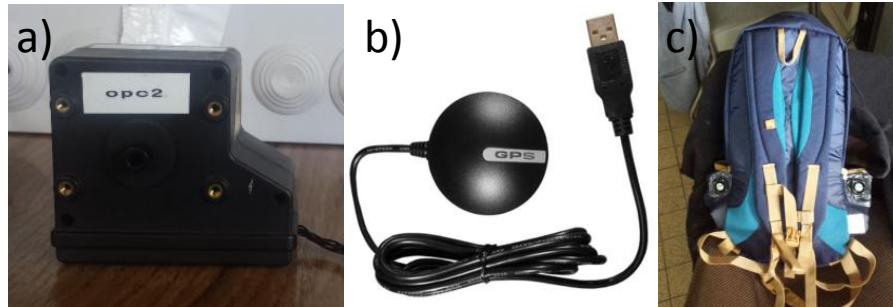


Fig. 1 – Illustration of the *a)* OPC-N2 Alphasense, *b)* GPS – model BU-353 and *c)* Backpack set up with two OPC mounted in the side pockets.

In order to evaluate the performance of the low-cost sensor, we compared measurements performed by OPC-N2 and a particle sizer, miniWRAS model 1371 - Mini Wide Range Aerosol Spectrometer (Grimm, 2017), arranged side by side. The miniWRAS instrument was considered as a reference instrument (Sousan *et al.*, 2016). The size range of miniWRAS is from  $0.01 \mu\text{m}$  to  $32 \mu\text{m}$  divided in 41 size channels and measurement data every minute (User Manual, Grimm, 2017) are provided. The measurements were performed on the rooftop of LOA (Laboratoire d'Optique Atmosphérique) at Lille University ( $50^{\circ}36'29''$  N,  $3^{\circ}8'25''$  E), at an elevation of 20 meters above ground.

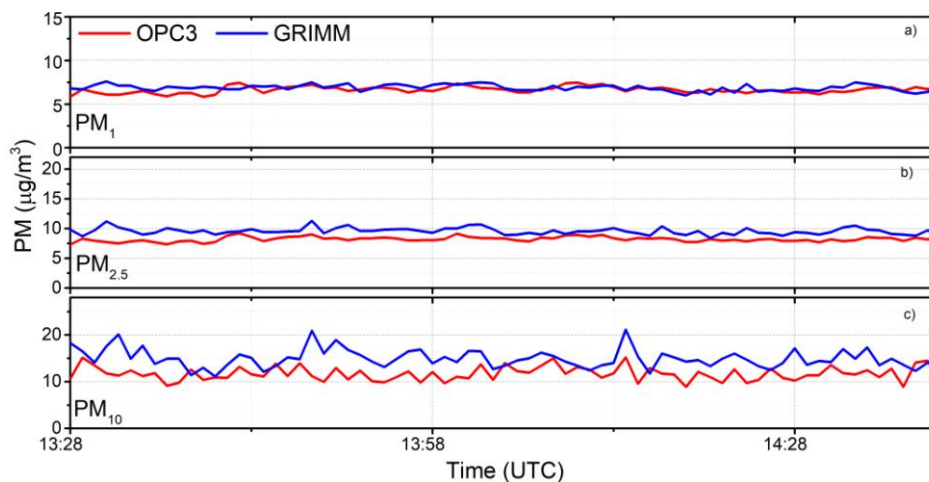


Fig. 2 – Illustration of the *(a)*  $\text{PM}_{10}$ , *(b)*  $\text{PM}_{2.5}$  and *(c)*  $\text{PM}_1$  mass concentration variations as depicted from OPC (red line) and mini WRAS (blue line) measurements in Villeneuve d'Ascq, France, on the roof of LOA on 13/07/2017.

Fig. 2 shows the derived PM mass concentration from OPC and mini-WRAS stationary measurements on 13 July 2017, 13:28 – 14:40 UTC. We can observe that the OPC-N2 describes the same variability in PM<sub>1</sub>, PM<sub>2.5</sub> and PM<sub>10</sub> concentrations as the miniWRAS and that the discrepancy is small. The linear fit between coincident measurements of both particle sizers show a good correlation with a Pearson's r factor of 0.98 for all PM<sub>10</sub>, PM<sub>2.5</sub> and PM<sub>1</sub> (not shown here). However, the slope values for PM<sub>10</sub>, PM<sub>2.5</sub> and PM<sub>1</sub> comparisons are 0.83, 0.75 and 0.7, respectively, meaning that the OPC-N2 slightly underestimated the PM mass concentrations, compared to GRIMM mini-WRAS.

### 3. Mobile Measurements in Lille

The measurements were performed in the city-center of Lille, Citadel of Lille, Vauban Park, Porte de Paris and Jean-Baptiste Lebas Park on 28 and 29 August 2017. For these two days the air-quality forecast models predicted a pollution event in Lille area (Atmo Hauts-de-France - Mesures des stations de surveillance de la qualité de l'air, 2018).

Fig. 3a shows the PM<sub>1</sub>, PM<sub>2.5</sub> and PM<sub>10</sub> mass concentration variations derived from measurements with the low-cost sensor OPC-N2. The recorded mass concentrations are higher in the first part of the day, (8:10 UTC- 11:40 UTC), in the range of 22 - 80  $\mu\text{g}/\text{m}^3$ , 25 - 100  $\mu\text{g}/\text{m}^3$  and 32 - 115  $\mu\text{g}/\text{m}^3$  for PM<sub>1</sub>, PM<sub>2.5</sub> and PM<sub>10</sub>, respectively. From 12:00 UTC to 14:30 UTC, the particle concentration starts to decrease; however some peaks can be observed in Fig. 3, most probably due to the city traffic.

The next day, 29 August 2017, measurements were performed in the center of Lille, Citadelle of Lille, Vauban Park. The results shown in Fig. 3b indicate that the values of PM concentration are lower compared to previous day. The recorder mass concentrations are in the range of 5 - 20  $\mu\text{g}/\text{m}^3$ , 7 - 25  $\mu\text{g}/\text{m}^3$  and 15 - 60  $\mu\text{g}/\text{m}^3$ , for PM<sub>1</sub>, PM<sub>2.5</sub> and PM<sub>10</sub>, respectively. Moreover, a peak in mass concentration at 11:40 UTC can be observed, corresponding to the passage close to a building site, when PM<sub>1</sub>, PM<sub>2.5</sub> and PM<sub>10</sub> values are around 80, 200 and 1500  $\mu\text{g}/\text{m}^3$ , respectively.

On 28 August 2017, in Lille city center the highest values were recorded, exceeding 100  $\mu\text{g}/\text{m}^3$  for PM<sub>10</sub>, values that decreased during the day to around 20-40  $\mu\text{g}/\text{m}^3$  for PM<sub>10</sub> in the green space areas, such as Citadel of Lille, Vauban Park, Jean-Baptiste Lebas Park. On 29 August 2017, PM<sub>x</sub> concentrations for the same time interval were, on average, around 25  $\mu\text{g}/\text{m}^3$ . The highest values are recorded in the city center, from 8:00 UTC to 9:00 UTC, decreasing during the day. In Vauban Park and Citadel of Lille, only PM<sub>10</sub> mass concentration presented variations, while PM<sub>1</sub> and PM<sub>2.5</sub> contributions remained stable. In the university campus located in Villeneuve d'Ascq, the PM's mass concentration values were lower than 25  $\mu\text{g}/\text{m}^3$ , showing low levels of air pollution.

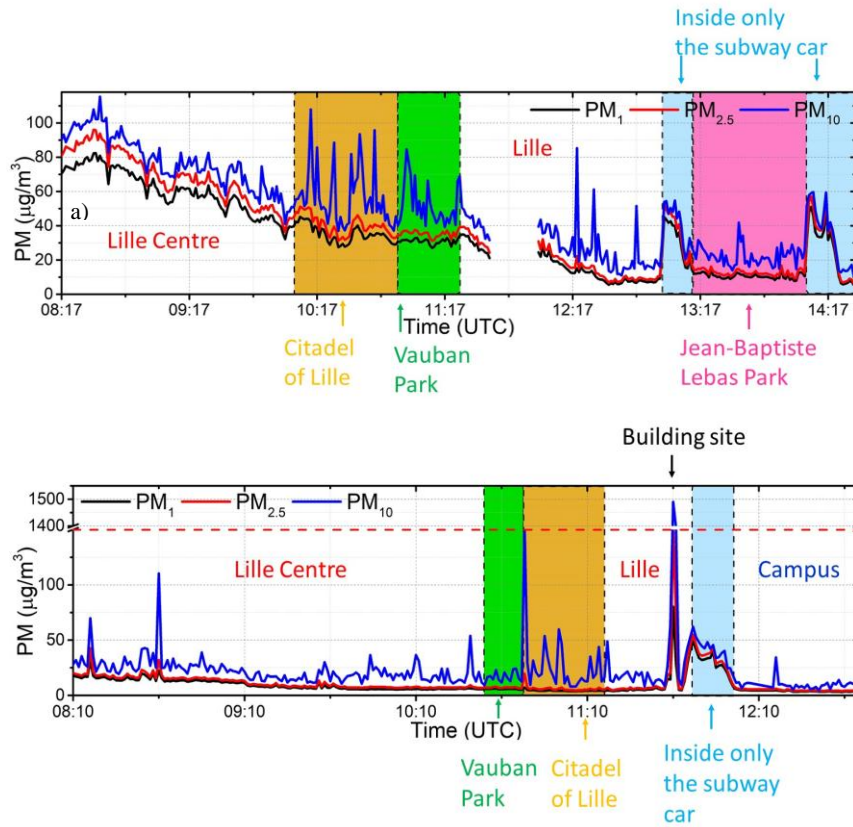


Fig. 3 – Illustration of the PM<sub>1</sub>, PM<sub>2.5</sub> and PM<sub>10</sub> mass concentration variations as measured by OPC-N2. *a)* Measurements in Lille on 28/08/2017. The black, red and blue lines represent the mass concentrations for PM<sub>1</sub>, PM<sub>2.5</sub> and PM<sub>10</sub>, respectively. *b)* Measurements in Lille on 29/08/2017. The black, red and blue lines represent the mass concentration for PM<sub>1</sub>, PM<sub>2.5</sub> and PM<sub>10</sub>, respectively. The red dashed line marks a break from 150 to 1400  $\mu\text{g}/\text{m}^3$ .

A spatial visualization of the polluted regions in the urban agglomeration of Lille can be achieved by plotting the data on Google Earth maps. Fig. 4 illustrates the map of PM<sub>10</sub> mass concentrations recorded on 28 and 29 August 2017. On 28 August 2017, we can observe that in Lille city center, the PM<sub>10</sub> mass concentrations are in the range of 90 – 100  $\mu\text{g}/\text{m}^3$  and they start to decrease down to 40  $\mu\text{g}/\text{m}^3$  in green space areas. However, the PM<sub>10</sub> concentrations on 29 August 2017, on the same route, decreased considerably. In some places, the PM<sub>10</sub> concentrations can exceed 100  $\mu\text{g}/\text{m}^3$ , which can be explained by local emission sources, such as construction sites or other activities that suspend more particles in the atmosphere. This time, on 29

August, both in Lille city-center and in green space areas, the values are in the  $20 - 40 \mu\text{g}/\text{m}^3$  range, considerably lower than the previous day.

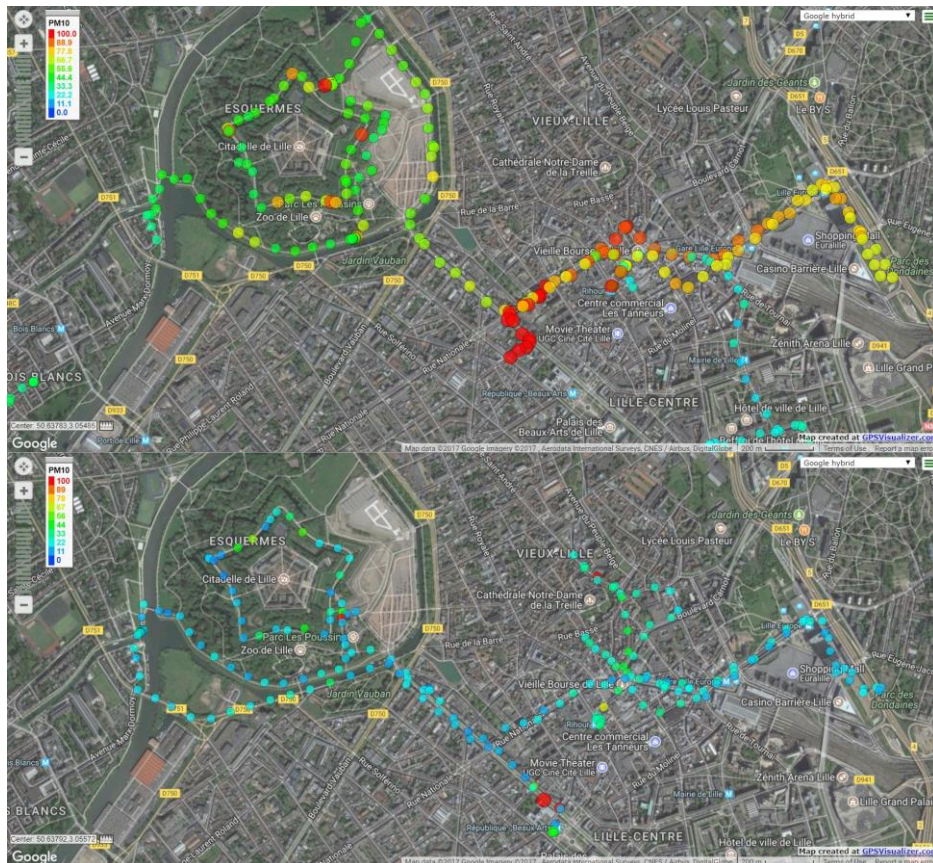


Fig. 4 – Illustration of the spatial variability of  $\text{PM}_{10}$  concentrations as measured by OPC-N2. Measurements in the urban agglomeration of Lille on a) 28/08/2017, b) 29/08/2017. The color scale is from 0 to  $100 \mu\text{g}/\text{m}^3$ , with a step of  $10 \mu\text{g}/\text{m}^3$ , from blue to red. The values exceeding the upper limit are also represented in red.

The measurements performed in Lille center and green space areas revealed that there was a significant level of air pollution on 28 August 2017 and the regions affecting notably the city center and the green space areas, *e.g.* Citadel of Lille and Vauban Park. Of course, one must also consider the time scale of the conducted field measurements and the temporal atmospheric variability. The second day, on 29 August 2017, the levels of PM mass concentration were at a quarter of the previous day levels. Higher winds that dispersed the pollutants and “cleaned” the atmosphere can explain the lower PM’s concentrations.

#### 4. Conclusions

On-road mobile measurements presented in this study use techniques that involve low-cost (about 300 – 400 euro) particle sensors (OPC) for the measurement of particulate matter (PM) concentrations. The reliability of OPC measurements was checked against a reference instrument, GRIMM mini-WRAS aerosol spectrometer, in this study, and results show good agreement between the two instruments.

The setup equipment for mobile measurements is quite simple, consisting of a low-cost particle sensor (OPC), a GPS and a laptop, mounted in a backpack and carried by a person to conduct on foot measurements. Spatial variability is then illustrated on Google Earth maps using the GPS data.

Mobile measurements were conducted in Lille urban agglomeration, France, in the period August-September 2017. Examples shown here illustrate a high variability between two days, 28 and 29 August, at an urban scale. A pollution event on 28 August was investigated at a fine spatial scale using the low cost OPC.  $PM_{10}$  concentrations exceeded  $100 \mu\text{g}/\text{m}^3$  in the city center in the morning, while  $PM_1$  and  $PM_{2.5}$  concentrations recorded in green space areas were in the range of  $30\text{-}50 \mu\text{g}/\text{m}^3$ . The fine particles are known to be more dangerous for health and this is particularly important for persons doing physical exercises in these green space areas.

This type of measurements can be used in studies of the human exposure to pollutants in urban and rural areas. The advantage is that any user can perform this type of measurements. Of course, the measurement methodology could be improved (e.g. using smartphones for multiple measurements in the same time) and preliminary data could alert the population to avoid certain areas during particular time intervals based on  $PM_x$  concentrations. Since on road measurements indicate that human exposure to pollutants can be quite variable, more real-time measurements, accessible to the population, would be of real importance.

**Acknowledgements.** This work was supported by the ERASMUS+ and by the Romanian Space Agency (ROSA) within Space Technology and Advanced Research (STAR) Program (Project no.: 162/20.07.2017). Laboratoire d'Optique Atmosphérique and Service National d'Observation PHOTONS/AERONET from INSU/CNRS are acknowledged for their support during ERASMUS internship.

#### REFERENCES

- Bezantakos S., Schmidt-Ott F., Biskos G., *Performance Evaluation of the Cost-Effective and Lightweight Alphasense Optical Particle Counter for Use Onboard Unmanned Aerial Vehicles*, *Aerosol Science and Technology*, 1-8 (2017), <https://doi.org/10.1080/02786826.2017.1412394>.

- Crilly L.R., Shaw M., Pound R., Kramer L.J., Price R., Young S., Pope F.D. *Evaluation of a Low-Cost Optical Particle Counter (Alphasense OPC-N2) for Ambient Air Monitoring*, *Atmos. Meas. Tech*, **11**, 709-720 (2018), <https://doi.org/10.5194/amt-11-709-2018>.
- Crippa P., Castruccio S., Archer-Nicholls S., Lebron G.B., Kuwata M. *et al.*, *Population Exposure to Hazardous Air Quality Due to the 2015 Fires in Equatorial Asia*, *Scientific Reports*, **6**, 37074 (2016), <https://doi.org/10.1038/srep37074>.
- de Meij A., Pozzer A., Lelieveld J., *Trend Analysis in Aerosol Optical Depths and Pollutant Emission Estimates Between 2000 and 2009*, *Atmospheric Environment*, **51**, 75-85 (2012), <https://doi.org/10.1016/j.atmosenv.2012.01.059>.
- Fuzzi S., Baltensperger U., Carslaw K., Decesari S., Denier Van Der Gon H. *et al.*, *Particulate Matter, Air Quality and Climate: Lessons Learned and Future Needs*, *Atmospheric Chemistry and Physics*, **15**, 14, 8217-8299 (2015), <https://doi.org/10.5194/acp-15-8217-2015>.
- Ielpo P., Paolillo V., de Gennaro G., Dambruoso P.R., *PM10 and Gaseous Pollutants Trends from Air Quality Monitoring Networks in Bari Province: Principal Component Analysis and Absolute Principal Component Scores on a Two Years and Half Data Set*, *Chemistry Central Journal*, **8**, 1, 14 (2014), <https://doi.org/10.1186/1752-153X-8-14>.
- Ignotti E., Valente J.G., Longo K.M., Freitas S.R., Hacon S.D., Netto P.A., *Impact on Human Health of Particulate Matter Emitted from Burnings in the Brazilian Amazon Region*, *Revista de Saude Publica*, **44**, 1, 121-130 (2010), <https://doi.org/10.1590/S0034-89102010000100013>.
- Johnson K.S., Zuberi B., Molina L.T., Molina M.J., Iedema M.J. *et al.*, *Processing of Soot in an Urban Environment: Case Study from the Mexico City Metropolitan Area*, *Atmospheric Chemistry and Physics*, **5**, 3033-3043 (2005), <https://doi.org/10.5194/acpd-5-5585-2005>.
- Kinne S., Schulz M., Textor C., Guibert S., Balkanski Y. *et al.*, *An AeroCom Initial Assessment – Optical Properties in Aerosol Component Modules of Global Models*, *Atmospheric Chemistry and Physics*, **6**, 7, 1815-1834 (2006), <https://doi.org/10.5194/acp-6-1815-2006>.
- Lieberman A., *Optical Particle Counter Operating Procedures, Calibration and Correlation Methods*, In *Contamination Control and Cleanrooms*, Boston, MA: Springer US., 331-349 (1992), [https://doi.org/10.1007/978-1-4684-6512-9\\_26](https://doi.org/10.1007/978-1-4684-6512-9_26).
- Mallet M., Dulac F., Formenti P., Nabat P., Sciare J. *et al.*, *Overview of the Chemistry-Aerosol Mediterranean Experiment/Aerosol Direct Radiative Forcing on the Mediterranean Climate (Charmex/ADRIMED) Summer 2013 Campaign*, *Atmospheric Chemistry and Physics*, **16**, 2, 455-504 (2016), <https://doi.org/10.5194/acp-16-455-2016>.
- Mann G.W., Carslaw K.S., Reddington C.L., Pringle K.J., Schulz M. *et al.*, *Intercomparison and Evaluation of Global Aerosol Microphysical Properties Among AeroCom Models of a Range of Complexity*, *Atmospheric Chemistry and Physics*, **14**, 9, 4679-4713 (2014), <https://doi.org/10.5194/acp-14-4679-2014>.
- Müller A., Miyazaki Y., Aggarwal S.G., Kitamori Y., Boreddy S.K.R., Kawamura K., *Effects of Chemical Composition and Mixing State on Size-Resolved Hygroscopicity and Cloud Condensation Nuclei Activity of Submicron Aerosols at a Suburban Site in Northern Japan in Summer*, *Journal of Geophysical*

- Research: Atmospheres (2017), 1-18. <https://doi.org/10.1002/2017JD027286>.
- Nessler R., Weingartner E., Baltensperger U., *Effect of Humidity on Aerosol Light Absorption and its Implications for Extinction and the Single Scattering Albedo Illustrated for a Site in the Lower Free Troposphere*, Journal of Aerosol Science, **36**, 8, 958-972 (2005).
- Niemi J.V., Saarikoski S., Tervahattu H., Mäkelä T., Hillamo R. *et al.*, *Changes in Background Aerosol Composition in Finland During Polluted and Clean Periods Studied by TEM/EDX Individual Particle Analysis*, Atmospheric Chemistry and Physics Discussions, **6**, 4, 6753-6799 (2006), <https://doi.org/10.5194/acpd-6-6753-2006>.
- Pöschl U., *Atmospheric Aerosols: Composition, Transformation, Climate and Health Effects*, Angewandte Chemie - International Edition, **44**, 46, 7520-7540 (2005), <https://doi.org/10.1002/anie.200501122>.
- Sousan S., Koehler K., Hallett L., Peters T.M. *Evaluation of the Alphasense Optical Particle Counter (OPC-N2) and the Grimm Portable Aerosol Spectrometer (PAS-1.108)*, Aerosol Science and Technology, **50**, 12, 1352-1365 (2016), <https://doi.org/10.1080/02786826.2016.1232859>.
- Van de Hulst H.C., *Light Scattering by Small Particles* (1981).
- Yu F., Luo G., Ma X., *Regional and Global Modeling of Aerosol Optical Properties with a Size, Composition, and Mixing State Resolved Particle Microphysics Model*, Atmospheric Chemistry and Physics, **12**, 13, 5719-5736 (2012), <https://doi.org/10.5194/acp-12-5719-2012>.
- \* *Alphasense User Manual OPC-N2 Optical Particle Counter*, Issue 3 (2015), Retrieved from [www.alphasense.com](http://www.alphasense.com).
- \*\* Atmo Hauts-de-France - *Mesures des stations de surveillance de la qualité de l'air*, Retrieved February 8, 2018, from <http://www.atmo-hdf.fr/acceder-aux-donnees/mesures-des-stations.html?view=mesures>.
- \*\* *US GlobalSat Corporate* [WWW Document] (2014), Retrieved September 8, 2017, from <http://usglobalsat.com/p-62-bu-353-w.aspx#images/product/large/62.jpg>.
- \*\* *User manual, Grimm* (2017), Retrieved February 14, 2018, from <http://wiki.grimm-aerosol.de/index.php?title=IAQ-Mini-Wras-1371>.

MĂSURATORI MOBILE ALE DISTRIBUȚIEI GRANULOMETRICE  
ȘI ESTIMAREA CONCENTRAȚIILOR DE MASĂ CU UN SENZOR DE COST  
REDUS ÎN LILLE, NORDUL FRANȚEI

(Rezumat)

În general, în aglomerările urbane, calitatea aerului și nivelurile de poluare sunt evaluate de stațiile de monitorizare aflate în locații fixe. Cu toate acestea, concentrațiile de masă a particulelor (PM<sub>10, 2.5, 1</sub>) la nivelul suprafeței, care sunt periculoase pentru mediul înconjurător și pentru sănătate, pot fi foarte variabile în spațiu și timp chiar și la scară locală. Astfel, este necesar să se evalueze distribuția spațială a pulberilor de particule la scară spațială fină. Pentru aceasta, am efectuat măsurători mobile pe drumuri ale distribuțiilor granulometrice cu un senzor low-cost, Alphasense OPC-N2, pentru a estima PM<sub>10, 2.5, 1</sub>. Măsurările au fost efectuate în zonele urbane ale orașului Lille, în

---

nordul Franței. Aici, evidențiem gradientul nivelului de poluare dintre zonele mai mult și mai puțin populate. A fost găsit un nivel crescut de poluare în apropierea centrelor comerciale, unde  $PM_{10}$  poate fi mai mare de  $40 \mu\text{g}/\text{m}^3$ .



BULETINUL INSTITUTULUI POLITEHNIC DIN IAȘI  
Publicat de  
Universitatea Tehnică „Gheorghe Asachi” din Iași  
Volumul 64 (68), Numărul 1, 2018  
Secția  
MATEMATICĂ. MECANICĂ TEORETICĂ. FIZICĂ

## CORONARY ARTERY OCCLUSION EXPLAINED BY MEANS OF A FRACTAL MODEL

BY

VLAD GHIZDOVĂȚ<sup>1</sup>, IGOR NEDELCIUC<sup>2,\*</sup>, CIPRIANA ȘTEFĂNESCU<sup>1</sup>,  
ANDREI ZALA<sup>3</sup>, MARICEL AGOP<sup>4,5</sup> and NICOLAE DAN TESLOIANU<sup>6</sup>

<sup>1</sup>“Grigore T. Popa” University of Medicine and Pharmacy, Iași, Romania,  
Faculty of Medicine, Biophysics and Medical Physics Department

<sup>2</sup>Institute of Cardiovascular Disease “G.I.M. Georgescu”, Iași, Romania  
“Gheorghe Asachi” Technical University of Iași, Romania,

<sup>3</sup>Electrical Engineering Department

<sup>4</sup>Physics Department

<sup>5</sup>Academy of Romanian Scientists, București, Romania

<sup>6</sup>“St. Spiridon” University Hospital, Iași, Romania,  
Department of Cardiology

Received: March 8, 2018

Accepted for publication: April 23, 2018

**Abstract.** We prove through a fractal model that the blocking of the lumen of an absolutely healthy artery can happen as a result of the “stopping effect”, in the conditions of a normal sanguine circulation. Our fractal model was used for in vivo analyzes of ten clinical cases of patients with acute occlusive thrombus on an absolutely healthy artery. We present the two most relevant cases, with thrombus dimensions of 60 or more millimeters. Our theoretical results were verified by coronarography images.

**Keywords:** acute arterial occlusion; nonlinear dynamics; Bingham fluid; Scale Relativity Theory.

---

\*Corresponding author; *e-mail*: inedel@yahoo.com

## 1. Introduction

The acute arterial occlusion of an artery that has no significant preexistent lesions leads to dramatic consequences due to the lack of collateral substitutive circulation, as this kind of circulation usually develops within years, in the presence of hemodynamic significant stenosis (Hiatt *et al.*, 2004).

Classical models which explain this phenomenon take into account the cracking of an intimal atheroma plaque, the activation of the pro-thrombogenic cascade through the denudation of the endothelium and the formation in certain circumstances of a completely occlusive thrombus (Badimon and Vilahur, 2014; Toney *et al.*, 2014). At least one counterargument should be taken into consideration: why does an occlusive thrombus form so quickly in the absence of a stenosis, when the sanguine flux is unaltered? Why doesn't the "wash-out" phenomenon appear?

Without contradicting these usual models, we will prove through a fractal model (Popa *et al.*, 2015; Tesloianu *et al.*, 2015) that the blocking of the lumen of an absolutely healthy artery can happen as a result of the "stopping effect" (even in the absence of the at least disputable cracked and non-protrusive atheroma plaque), in the conditions of a normal sanguine circulation.

## 2. Theoretical Model

If we consider blood a Bingham-type rheological fluid, then

$$\tau = \tau_0 + \eta \frac{dv}{dr} \quad (1)$$

where  $\tau$  is the viscosity tangential unitary effort,  $\tau_0$  is the deformation tangential unitary effort,  $dv/dr$  is the velocity gradient with respect to the normal on the transversal section and  $\eta$  is the viscosity coefficient.

The mathematical procedure we used had the following steps:

i) determining the values of Reynolds' number for blood flow through the right coronary artery, using the following relation:

$$R_e = \frac{v_s D}{\eta} \quad (2)$$

where  $v_s$  is the minimum value of the average experimental systolic velocity of blood,  $D$  is the average experimental diameter of the right coronary artery, and  $\eta$  is the average kinetic viscosity coefficient of blood;

ii) determining the values of the loss coefficient of blood flow through the same artery, using Darcy's formula [6]:

$$\lambda = \frac{64}{R_e} = \frac{64\eta}{v_s D} \quad (3)$$

iii) determining the values of the pressure loss for blood flow, using the following relation (Bar-Yam, 1997):

$$\Delta p = \lambda \frac{L}{D} \rho \frac{v_d^2}{2} = 32\eta\rho \frac{L}{D^2} \frac{v_d^2}{v_s} \quad (4)$$

where  $L$  is the average length of the experimental thrombus,  $\rho$  is the average experimental blood density, and  $v_d$  is the maximum value of blood's average experimental systolic velocity;

iv) determining the theoretical dimension of a right coronary artery thrombus, using the relation:

$$D_t = \frac{4\tau_0 L}{\Delta p} = \frac{1}{8} \frac{v_s \tau_0 D^2}{\eta\rho v_d^2} \quad (5)$$

where  $\tau_0$  is the average experimental deformation stress of blood (Axinte *et al.*, 2014; Tesloianu *et al.*, 2014).

### 3. Results

Our fractal model (Popa *et al.*, 2015; Tesloianu *et al.*, 2015) was used for in vivo analyzes of ten clinical cases of patients with acute occlusive thrombus on an absolutely healthy artery. These cases were selected during a 2-year period (2013 – 2015). Patients with atrial fibrillation were excluded for preventing mismatch with thromboembolic acute coronary occlusion. Patients with patent foramen ovale (transesophageal echocardiography study performed) were excluded in order to avoid a paradoxically coronary embolism. IVUS (intravascular ultrasound) or coronary angio CT were not performed for these patients; even if some irregularities could be seen at an angiography, it is clear that there are no significant ulcerated atheroma plaques or major signs of parietal atherosclerosis. Also, in patients older than fifty years an absolutely normal coronary wall is more likely a utopia. We had EKG holter monitoring in all patients for exclusion of paroxysmal atrial fibrillation.

We present here the two most relevant cases (Fig. 1), with thrombus dimensions of 60 or more millimeters (for the other eight cases, the thrombus dimensions were between 30 and 60 mm). Our theoretical results were verified by coronarography images.

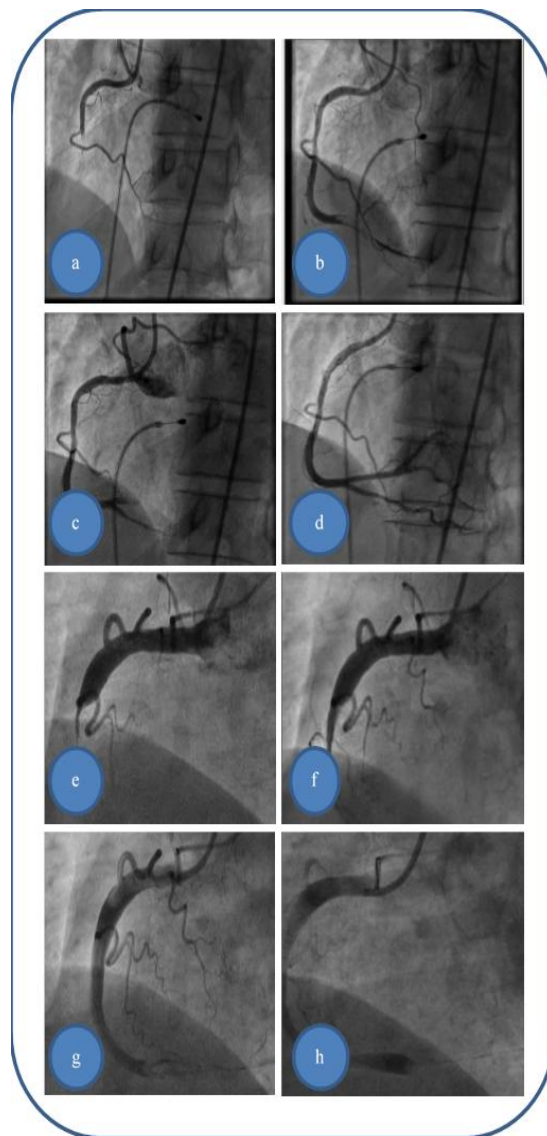


Fig. 1– Acute thrombus formation in apparently healthy artery with no evidence of plaque dissection like as a responsible lesion – different interventional approach stages: patient 1 (*a-d*), patient 2 (*e-f*).

i) Patient 1, 52 years old male patient, who was diagnosed with acute infer lateral ischemia; the coronary angiography revealed an acute occlusive thrombus (4-4.5 mm diameter and 60 – 80 mm length) at the junction between segments I and II of right coronary artery; after thrombus aspiration a distal thrombotic embolism appears with an apparently healthy artery (or possible

minimal lesion – no sign of plaque dissection) at the initial thrombus level; repeated thrombus aspiration at the level of secondary occlusion reveals the posterior descending branch and subsequently posterolateral branch; also, there was no evident coronary lesion responsible for the above stated pathological phenomena;

ii) Patient 2, 57 years old male patient who was diagnosed with acute inferior and poster lateral ischemia; coronary angiography revealed an acute occlusive thrombus extended from the beginning of right coronary artery segment II to crux (4.5 – 5 mm diameter and approx. 80 – 100 mm length), possible with extension to right posterior descending artery and poster lateral branches; unsatisfying results in term of distal TIMI flow (0-1) but with no evidence of significant atherosclerotic disease at the level of culprit zone.

We present in Table 1 the average experimental parameters of blood flow through the right coronary artery, used in our study, and also the average theoretical parameters of blood flow through the right coronary artery, obtained using our theoretical model (Popa *et al.*, 2015; Tesloianu *et al.*, 2015).

**Table 1**  
Average Experimental Parameters of Blood Flow Through the Right Coronary Artery for the Two Clinical Cases

Patient's age [years]	$D_e$ [mm]	$L$ [mm]	$\tau_0$ [N/m <sup>2</sup> ]	$v_d$ [cm/s]	$v_s$ [cm/s]	$\rho$ [kg/m <sup>3</sup> ]	$\eta$ [m <sup>2</sup> /s]
52	4	70	9/75 mm Hg	35 ± 11	24 ± 7	1060	3.04 x 10 <sup>-6</sup> at 36.5°C
57	5	90	7/83 mm Hg	35 ± 11	24 ± 7	1060	3.04 x 10 <sup>-6</sup> at 36.5°C
Observations			The method from (Sharif <i>et al.</i> , 2015) was used	The method from (Sharif <i>et al.</i> , 2015) was used	The method from (Malek <i>et al.</i> , 1999) was used	The method from (Malek <i>et al.</i> , 1999) was used	The method from (Sharif <i>et al.</i> , 2015) was used
$R_e$	$\lambda$	$\Delta p$ [N/m]	$D_t$ [mm]				
226	0.283	634	4.54				
283	0.226	457	5.52				

Legend:  $D$  – average experimental thrombus diameter;  $L$  – average experimental thrombus length;  $\tau_0$  – average experimental deformation stress as a function of diastolic pressure;  $v_d$  – average experimental diastolic velocity;  $v_s$  – average experimental systolic velocity;  $\rho$  – average experimental blood density;  $\eta$  – average experimental kinetic viscosity coefficient;  $R_e$  – Reynolds' number;  $\lambda$  – Darcy's loss coefficient;  $\Delta p$  – pressure loss;  $D_t$  – thrombus diameter determined using our model.

#### 4. Conclusions

We can see a good conformity between the values from the theoretical model with the experimental/real estimated values (Hiatt *et al.*, 2004; Tesloianu *et al.*, 2015) in coronary angiography we found in the two cases presented above. Due to the fact that our model can be extrapolated to every cylindrical structure, in our opinion similar phenomena can occur, at least theoretically, in every artery of similar dimensions and hydrodynamic regimen (brain, kidney, splanchnic system etc.).

We note that the same model can also be applied, because of its theoretical implications, in engineering and materials science, in various domains, such as the ones described in (Agape *et al.*, 2016; Agape *et al.*, 2017; Gaiginschi and Agape, 2016; Gaiginschi *et al.*, 2011; Gaiginschi *et al.*, 2014a; Gaiginschi *et al.*, 2014b; Gaiginschi *et al.*, 2017; Vornicu *et al.*, 2017).

#### REFERENCES

- Agape I., Gaiginschi L., Gaiginschi R., Baltagiu D., *Upon a Simple Method for Generating Transversal Profile of the Volumic Blower Rotor Used in Supercharging ICE*, Ingineria Automobilului, **38**, 22-25 (2016).
- Agape I., Gaiginschi L., Ianuş G., Cimpoesu N., *The Analysis of an Internal Combustion Engine Breakdown - Case Study*, IOP Conference Series: Materials Science and Engineering, **209**, 1, 012077 (2017).
- Axinte C.I., Baciuc C., Volovat S., Tesloianu D., Boros Z., Baciuc A., *Flow Dynamics Regimes via Nondifferentiability in Complex Fluids*, UPB. Sci Bull, **Series VII**, 233-242 (2014).
- Badimon L., Vilahur G., *Thrombosis Formation on Atherosclerotic Lesions and Plaque Rupture*, Journal of Internal Medicine, **276**, 618-632 (2014).
- Bar-Yam Y., *Dynamics of Complex Systems*, Addison-Wesley, Reading, 1997.
- Gaiginschi L., Agape I., *Upon an Issue of Correlation Between the Running Speed of Vehicles and Traffic Capacity of a Road Section*, IOP Conference Series: Materials Science and Engineering, **147**, 1, 012118 doi:10.1088/1757-899X/147/1/012118 (2016).
- Gaiginschi L., Gaiginschi R., Agape I., Hantoiu V., *Researches Regarding Impact Energy Dissipation by breaking for Front – Rear Collisions*, Ingineria Automobilului, **18**, 20-23 (2011).
- Gaiginschi L., Agape I., Sachelarie A., Girbaci M.A., *Virtual High Speed Diesel Engine – A Simulated Experiment, Part I: Combustion Dynamics*, Applied Mechanics and Materials, **659**, 189-194 (2014a).
- Gaiginschi L., Agape I., Sachelarie A., Girbaci M.-A., *Virtual High Speed Diesel Engine – A Simulated Experiment. Part II: The Influence of Polytropic Exponent upon Combustion Product Formation*, Applied Mechanics and Materials, **659**, pag 195-200 (2014b).

- Gaiginschi L., Agape I., Talif S., *Upon the Reconstruction of Accidents Triggered by Tire Explosion. Analytical Model and Case Study*, IOP Conf. Series: Materials Science and Engineering, **252**, 012016 doi:10.1088/1757-899X/252/1/012016 (2017).
- Hiatt W.R., Baumgartner I., Bluemke D.A., *Peripheral Manifestations of Atherothrombosis*. In: Topol J.E., Editor, Atlas of Atherothrombosis, Beijing, 2004, 109-110.
- Malek A.M., Alper S.L., Izumo S., *Hemodynamic Shear Stress and its Role in Atherosclerosis*, JAMA, **282**, 2035-2042 (1999).
- Popa R.F., Nedeff V., Lazăr G., Scurtu D., EvaL., Ochiuz L., *Bingham Type Behaviours in Complex Fluids. Stopper Type Effect*, Journal of Computational and Theoretical Nanoscience, **12**, 3178-3182 (2015).
- Sharif D., Sharif-Rasslan A., Shahla C., Khalil A., Rosenschein U., *Differences in Coronary Artery Blood Velocities in the Setting of Normal Coronary Angiography and Normal Stress Echocardiography*, Heart International, **10**, e6-e11 (2015).
- Toney M.I., Narula J., Kovacic J.C., *Year in Review: Advances in Understanding of Plaque Composition and Treatment Options*, Journal of the American College of Cardiology, **63**, 1604-1616 (2014).
- Tesloianu N.D., Ghizdovăţ V., Agop M., *Flow Dynamics via Non-Differentiability and Cardiovascular Disease. A Proposal for an Interdisciplinary Approach between Non-Differentiable Physics and Cardiovascular Morphopatology*, Scholars' Press, Saarbrücken, 2015.
- Tesloianu D., Vrajitoriu L., Costin A., Vasincu D., Timofte D., *Dispersive Behaviours in Biological Fluids. Applications II*, Bul. Inst. Polit. Iași, s. Mathematics. Theoretical Mechanics. Physics, **LX(LXIV)**, 3 (2014).
- Vornicu V., Ulian T., Rakosi E., Manolache Gh., Gaiginschi L., *Theoretical Model for Determination of the Spark Ignition Engine Thermo-Gasodynamic Parameters on Various Functional Conditions*, IOP Conference Series: Materials Science and Engineering, **252**, 1, 012073 doi:10.1088/1757-899X/252/1/012073 (2017).

## OCLUZIA ARTEREI CORONARIENE EXPLICATĂ PRIN INTERMEDIUL UNUI MODEL FRACTAL

(Rezumat)

Folosind un model fractal, se arată că ocluzia unei artere absolute sănătoase, în condițiile unei circulații sanguine normale, poate apărea ca urmare a acțiunii unui „opritor”. Acest model a fost folosit pentru studierea in vivo a unui număr de 10 cazuri clinice de tromboză ocluzivă în artere absolute sănătoase. Prezentăm cele mai relevante două cazuri, cu dimensiuni ale trombusului de peste 60 mm. Rezultatele teoretice obținute sunt validate de imaginile angiografice.



BULETINUL INSTITUTULUI POLITEHNIC DIN IAȘI  
Publicat de  
Universitatea Tehnică „Gheorghe Asachi” din Iași  
Volumul 64 (68), Numărul 1, 2018  
Secția  
MATEMATICĂ. MECANICĂ TEORETICĂ. FIZICĂ

## COHERENCE IN FRACTAL STRUCTURES

BY

VLAD GHIZDOVĂȚ, MIHAI MARIUS GUȚU\* and  
CIPRIANA ȘTEFĂNESCU

“Grigore T. Popa” University of Medicine and Pharmacy, Iași, Romania,  
Faculty of Medicine, Biophysics and Medical Physics Department

Received: March 1, 2018

Accepted for publication: April 16, 2018

**Abstract.** We use the Scale Relativity Theory formalism in an arbitrary constant fractal dimension to show that for a two-dimensional non-differentiable and non-coherent fluid, for which we consider its entities as vortex-type objects, the coherence mechanism induces vortices streets. Moreover, if the fluid bears self-constraints from the two planes, the attractive or repulsive interaction force between the two planes can be determined. As a result, a Casimir-type effect at small scales and a Tiffet-type effect at large scales can appear. At nanoscale, these findings could explain the fractional or integer quantum Hall effect in graphenes.

**Keywords:** Scale Relativity Theory; structure coherence; Casimir-type effect; Tiffet-type effect; fractional or integer quantum Hall effect; graphenes.

### 1. Introduction

Nonlinearity manifests itself under many forms. One of these, the coherent structures, is of high interest. These structures can appear from small scales (nanoscale and mesoscopic scale) to large scales (infragalactic scale and extragalactic scale). For example, for small scale turbulence, the evidence of high-vorticity small-size filaments which were observed in Navier-Stokes

---

\*Corresponding author; *e-mail*: misugutu@yahoo.fr

equations simulations has provided significant theoretical and experimental data (Kawahara and Kida, 2004; Reguera *et al.*, 2008). Moreover, pattern formation and spatio-temporal structures are also prominent in fluid dynamics, dendritic growth, and also chemo-biological phenomena. In addition, granular flow and fracture dynamics are new theoretical fields, which had given rise to numerous problems with important nonlinear and statistical aspects, and they will certainly be of great importance in the coming years (Reguera *et al.*, 2008). These same aspects can also be encountered at large scale in the forming processes of cosmic structures (Kauffmann *et al.*, 1993; Schive *et al.*, 2014).

The role coherence plays in structure formation at various scales is presented in (Gottlieb *et al.*, 2004; Munceleanu *et al.*, 2011; Timofte *et al.*, 2011). More recently, the same topic has been discussed in various models of biological systems in (Tesloianu, 2015; Tesloianu *et al.*, 2015), and particularly for blood assimilated to a complex fluid.

In this work we want to show that in the case of a complex fluid, no matter the scale, coherence induces interaction between the complex fluids' structural units.

## 2. Short Reminder on the Differentiable-Non-Differentiable Scale Transition Equations

The dynamics of the differentiable-non-differentiable scale transition at nanoscale are described as follows (Agop and Casian-Botez, 2015):

i) the specific momentum conservation law associated to differentiable-non-differentiable scale transition:

$$\partial_t \mathbf{V} + \mathbf{V} \cdot \nabla \mathbf{V} - D(dt)^{\left(\frac{2}{D_F}\right)^{-1}} \Delta \mathbf{V} = 2\mathbf{V}_F \cdot \nabla \mathbf{V}_F + 2D(dt)^{\left(\frac{2}{D_F}\right)^{-1}} \nabla \mathbf{V}_F \quad (1)$$

ii) the states density conservation law associated to differentiable-non-differentiable scale transition:

$$\partial_t \rho + (\mathbf{V} \cdot \nabla) \rho - D(dt)^{\left(\frac{2}{D_F}\right)^{-1}} \Delta \rho = 0 \quad (2)$$

In relations (1) and (2)  $\mathbf{V}$  is the velocity associated to differentiable-non-differentiable scale transition

$$\mathbf{V} = \mathbf{V}_D - \mathbf{V}_F \quad (3)$$

$\mathbf{V}_D$  is the differentiable and scale independent velocity,  $\mathbf{V}_F$  is the non-differentiable and scale dependent velocity (Nottale, 1993; Nottale, 2011),

$\mathbf{V} \cdot \nabla \mathbf{V}$  is the convective-type term,  $D(dt)^{\left(\frac{2}{D_F}\right)^{-1}} \Delta \mathbf{V}$  is the dissipative-type

term,  $D_F$  is the fractal dimension of the motion curves,  $dt$  is the scale resolution and  $D$  is the specific coefficient associated to the differentiable-non-differentiable scale transition. For  $D_F$  we can accept any definition (Kolmogorov fractal dimension, Hausdorff-Beskovici fractal dimension (Mandelbrot, 1983) etc.), but once a definition is set, it has to be constant over the entire theoretical model for the involved dynamics.

If the motions at non-differentiable scale are irrotational, *i.e.*  $\nabla \times \mathbf{V}_F = 0$  we can choose  $\mathbf{V}_F$  of the form

$$\mathbf{V}_F = D(dt)^{\left(\frac{2}{D_F}\right)^{-1}} \nabla \ln \phi \quad (4)$$

with  $\ln \phi$  the non-differentiable velocity scalar potential.

In the particular case  $\phi \equiv \rho$  the right-side term from Eq. (1),

$$\begin{aligned} & 2 \left[ \mathbf{V}_F \cdot \nabla \mathbf{V}_F + D(dt)^{\left(\frac{2}{D_F}\right)^{-1}} \Delta \mathbf{V}_F \right] \equiv \\ & \equiv -2 \nabla \left[ -\frac{\mathbf{V}_F^2}{2} - D(dt)^{\left(\frac{2}{D_F}\right)^{-1}} \nabla \cdot \mathbf{V}_F \right] \equiv -\nabla \bar{Q} \end{aligned} \quad (5)$$

where  $\bar{Q}$  is the specific non-differentiable potential associated to the differentiable-non-differentiable scale transition,

$$\bar{Q} \equiv -\mathbf{V}_F^2 - 2D(dt)^{\left(\frac{2}{D_F}\right)^{-1}} \nabla \cdot \mathbf{V}_F \quad (6)$$

can be correlated with the tensor

$$\tau_{\mu\nu} \equiv 4D^2(dt)^{\left(\frac{4}{D_F}\right)^{-2}} \rho \nabla_\mu \nabla_\nu \ln \rho \quad (7)$$

by means of relation

$$\nabla \hat{\tau} + \rho \nabla \bar{Q} \equiv 0 \quad (8)$$

For „fluid” behaviours at differentiable-non-differentiable scale transition of isentropic type Eq. (7) becomes (Lifshietis and Landau, 1987)

$$\tau_{\mu\nu} = -p \delta_{\mu\nu} \quad (9)$$

where  $p$  is the pressure and

$$\delta_{\mu\nu} = \begin{cases} 1 & \mu = \nu \\ 0 & \mu \neq \nu \end{cases} \quad (10)$$

Next, we want to demonstrate that the above-defined pressure can generate either attractive, or repulsive force fields. In order to accomplish we must firstly consider that the velocity field is a cnoidal-type one (for mode details on the subject, see (Casian-Botez and Agop, 2015)).

### 3. Chaoticisation Through Non-Differentiability

All physical variables quantities, which are dependent on spatial-temporal coordinates and resolution scales (*i.e.* fractal variables), can be extended on a complex manifold by means of chaoticisation through non-differentiability (Nottale, 1993; Nottale, 2011). As an example, in the case of real space, the scalar velocity potential can be replaced with a “state function” from the fractal space (with probabilistic meanings of state density) through such an extension. Thus, the “state function’s” form can be determined through self-similarity that characterizes fractal variables (Aronstein and Stroud, 1997; Cristescu, 2008): if, in the real space, the one-dimensional velocity is of a cnoidal type (more details on this subject can be found in (Casian-Botez and Agop, 2015)), then, in the fractal space, the “state function” will also be cnoidal, if we use a suitable selection of a normalization factor.

Let us now consider a two-dimensional non-differentiable and non-coherent fluid. Then its entities, assimilated to vortex-type objects, are structured as a two-dimensional lattice, as can be seen in Fig. 1.

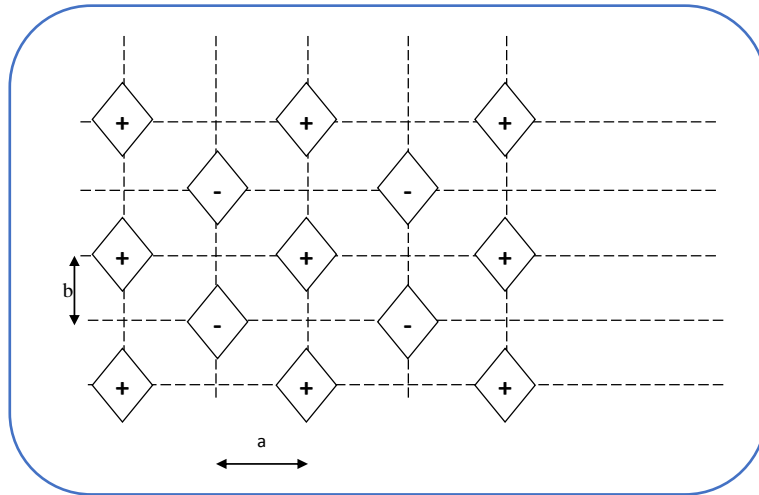


Fig. 1 – A two-dimensional lattice of vortex-type objects.

Then, taking into consideration the facts presented above (the cnoidal mode which is assimilated to a Toda-type nonlinear lattice (Cristescu, 2008; Toda, 1989) and the self-similarity property of physical variables) the “state function” has the expression

$$\Psi = cn(\bar{v}, s) \quad (11)$$

with

$$\begin{aligned} \bar{v} &= \frac{K}{a} \bar{u}, \bar{u} = \xi + i\eta, \frac{K}{a} = \frac{K'}{b}, \\ K &= \int_0^{\frac{\pi}{2}} \frac{d\varphi}{\left(1 - \bar{k}^2 \sin^2 \varphi\right)^{\frac{1}{2}}}, K' = \int_0^{\frac{\pi}{2}} \frac{d\varphi}{\left(1 - \bar{k}'^2 \sin^2 \varphi\right)^{\frac{1}{2}}}, \\ \bar{k}^2 + \bar{k}'^2 &= 1 \end{aligned} \quad (12a-f)$$

In relations (12 a-f)  $K$ ,  $K'$  are the complete elliptic integrals of the first kind of modulus  $\bar{k}$ <sup>37</sup> and  $a$ ,  $b$  are the constants of the vortex lattice (Armitage and Eberlein, 2006).

If we apply this formalism to a complex plane (for details see (Lifshietis and Landau, 1987)) and using the following equation

$$\Psi = e^{Q(\bar{u})/\Gamma} \equiv cn(\bar{v}; \bar{k}) \quad (13)$$

we induce the scalar complex potential of the complex velocity field

$$Q(\bar{u}) = \Gamma \ln \left[ cn(\bar{v}; \bar{k}) \right] \quad (14)$$

with  $\Gamma$  the vortex constant.

Based on (14) the complex velocity field can then be defined as

$$V_\xi - iV_\eta = \frac{dQ(\bar{u})}{d\bar{u}} = -\frac{\Gamma K}{a} \frac{\operatorname{sn}(\bar{v}; \bar{k}) \operatorname{dn}(\bar{v}; \bar{k})}{\operatorname{cn}(\bar{v}; \bar{k})} \quad (15)$$

or, using the notations (Armitage and Eberlein, 2006)

$$\begin{aligned} \bar{s} &= \operatorname{sn}(\bar{\alpha}; \bar{k}), \bar{c} = \operatorname{cn}(\bar{\alpha}; \bar{k}), \bar{d} = \operatorname{dn}(\bar{\alpha}; \bar{k}), \\ \bar{\alpha} &= \frac{K}{a} \xi, \bar{s}_1 = \operatorname{sn}(\bar{\beta}, \bar{k}'), \\ \bar{c}_1 &= \operatorname{cn}(\bar{\beta}, \bar{k}'), \bar{d}_1 = \operatorname{dn}(\bar{\beta}, \bar{k}'), \bar{\beta} = \frac{K}{a} \eta \end{aligned} \quad (16a-h)$$

$$\begin{aligned} V_\xi - iV_\eta &= -\frac{\Gamma K}{a} \frac{\bar{s}\bar{c}\bar{d} \left[ \bar{c}_1^{-2} (\bar{d}_1^{-2} + \bar{k}^2 \bar{c}^2 \bar{s}_1^{-2}) - \bar{s}_1^{-2} \bar{d}_1^{-2} (\bar{d}^2 \bar{c}_1^{-2} - \bar{k}^2 \bar{s}^2) \right]}{\bar{s}\bar{c}\bar{d} \left[ \bar{c}_1^{-2} (\bar{d}_1^{-2} + \bar{k}^2 \bar{c}^2 \bar{s}_1^{-2}) - \bar{s}_1^{-2} \bar{d}_1^{-2} (\bar{d}^2 \bar{c}_1^{-2} - \bar{k}^2 \bar{s}^2) \right]} \\ &\quad - i \frac{\Gamma K}{a} \frac{\bar{s}_1 \bar{c}_1 \bar{d}_1 \left[ \bar{c}^{-2} (\bar{d}^2 \bar{c}_1^{-2} - \bar{k}^2 \bar{s}^2) + \bar{s}^2 \bar{d}^2 (\bar{d}_1^{-2} + \bar{k}^2 \bar{c}^2 \bar{s}_1^{-2}) \right]}{(1 - \bar{d}^2 \bar{s}_1^{-2}) (\bar{c}^2 \bar{c}_1^{-2} + \bar{s}^2 \bar{d}^2 \bar{s}_1^{-2} \bar{d}_1^{-2})} \end{aligned} \quad (17)$$

Since

$$\begin{aligned} \operatorname{cn}(\bar{v} + \bar{\Omega}) &= \operatorname{cn}(\bar{v}) \\ \bar{\Omega} &= 2(2m+1)K + 2inK' \\ m, n &= \pm 1, \pm 2, \dots \end{aligned} \quad (18a-c)$$

for  $\bar{k} \rightarrow 0, \bar{k}' \rightarrow 1$  and  $\bar{k} \rightarrow 1, \bar{k}' \rightarrow 0$  limits, the initially non-coherent fluid (with the amplitudes and phases of its entities independent) becomes coherent (i.e. the amplitudes and phases of its entities are starting to be correlated). These types of dynamics can be seen in Figs. 2 *a-f*: it results that the coherence of the fluid reduces to its ordering on vortices streets – see Figs. 2 *a, b* for vortices streets aligned with the  $O\xi$  axis and Figs. 2 *e, f* for vortices streets aligned with the  $O\eta$  axis.

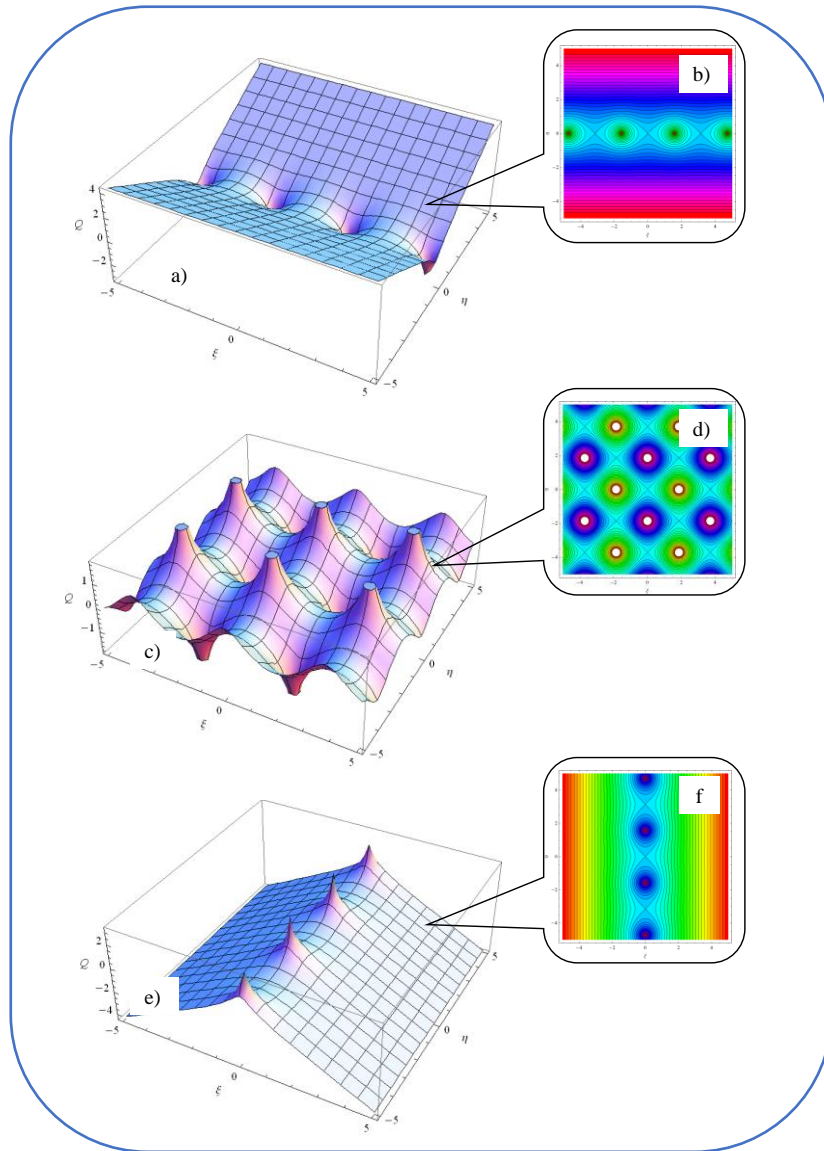


Fig. 2 – Three-dimensional (a, c, e) and two-dimensional (b, d, f) real part of the potential velocity field for different nonlinearity degrees ( $s = 0.1$  – a, b;  $s = 0.5$  – c, d;  $s = 1$  – e, f).

In this manner, if we consider that the state density is constant, the difference between self-dissipation and self-convection generates, through a self-pressure gradient, the self-force:

$$\frac{1}{\rho} \nabla p = \Gamma \Delta V - \mathbf{V} \cdot \Delta \mathbf{V} \quad (19)$$

or, in the  $\xi, \eta$  coordinates plane

$$\begin{aligned} \frac{\partial p}{\partial \xi} &= \rho \Gamma \left( \frac{\partial^2 V_\xi}{\partial \xi^2} + \frac{\partial^2 V_\xi}{\partial \eta^2} \right) - \rho \left( V_\xi \frac{\partial V_\xi}{\partial \xi} + V_\eta \frac{\partial V_\xi}{\partial \eta} \right) \\ \frac{\partial p}{\partial \eta} &= \rho \Gamma \left( \frac{\partial^2 V_\eta}{\partial \xi^2} + \frac{\partial^2 V_\eta}{\partial \eta^2} \right) - \rho \left( V_\xi \frac{\partial V_\eta}{\partial \xi} + V_\eta \frac{\partial V_\eta}{\partial \eta} \right) \end{aligned} \quad (20a, b)$$

Then, after employing a quite long but elementary calculus one gets from (20a,b), through the degenerations:

$$\text{i) } \bar{k} = 0, \bar{k}' = 1, K = \frac{\pi}{2}, K' = \infty$$

$$\begin{aligned} p_\eta(\bar{\alpha}_1) &= -p_0 \sin h^2 \left( \frac{\pi l_1}{2a} \right) \frac{1 - \tan^2 \bar{\alpha}_1}{\cos(2\bar{\alpha}_1) + \cos h \left( \frac{\pi l_1}{2a} \right)} \\ p_\xi(\bar{\beta}_1) &= -p_0 \sin^2 \left( \frac{\pi l_2}{2a} \right) \frac{1 - \tan h^2 \bar{\beta}_1}{\cos \left( \frac{\pi l_2}{2a} \right) + \cos h(2\bar{\beta}_1)} \end{aligned} \quad (21a, b)$$

with

$$p_0 = \rho \left( \frac{\pi \Gamma}{a} \right)^2, \bar{\alpha}_1 = \frac{\pi \xi}{2a}, \bar{\beta}_1 = \frac{\pi \eta}{2a} \quad (22a-c)$$

$$\text{ii) } \bar{k} = 1, \bar{k}' = 0, K = \infty, K' = \frac{\pi}{2}$$

$$\begin{aligned} p_\eta(\bar{\alpha}_1) &= -p_0 \sin^2 \left( \frac{\pi l_1}{2b} \right) \frac{1 + \tan h^2 \bar{\alpha}_1}{\cos \left( \frac{\pi l_1}{b} \right) + \cos h(2\bar{\alpha}_1)} \\ p_\xi(\bar{\beta}_1) &= -p_0 \sinh^2 \left( \frac{\pi l_2}{2b} \right) \frac{1 - \tan^2 \bar{\beta}_1}{\cos(2\bar{\beta}_1) + \cos h \left( \frac{\pi l_2}{2b} \right)} \end{aligned} \quad (23a, b)$$

with

$$p_0 = \rho \left( \frac{\pi \Gamma}{2b} \right)^2, \bar{\alpha}_1 = \frac{\pi \xi}{2b}, \bar{\beta}_1 = \frac{\pi \eta}{2b} \quad (24a-c)$$

In relations (21a, b) – (24a-c)  $l_1$  and  $l_2$  are the elementary space intervals as considered on the  $O\eta$  and  $O\xi$  axis, respectively (Fig. 3). As a result, we can state that the non-differentiability and coherence properties of the fluid, due to self-constraints, generate pressure along the  $O\xi$  and  $O\eta$  axis.

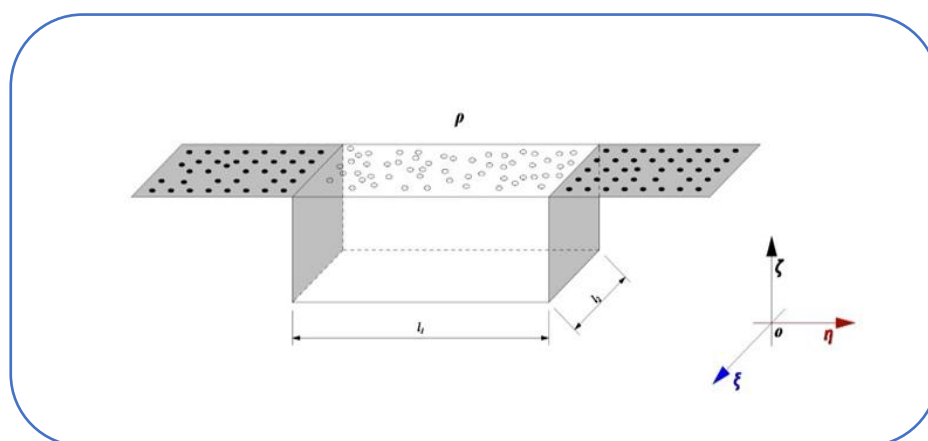


Fig. 3 – The fluid between two parallel planes, with its entities assimilated to vortex – type objects.

Let us now envision a fluid with a vortex lattice bounded by two parallel and infinitely thin liquid planes in the  $\xi O\zeta$  plane, at a distance  $l_1$  of each other. According to the facts we presented, if the fluid bears self-constraints from these two planes, then on their normal axis (here,  $O\eta$  axis), a coherent structure of vortex street type is induced. Consequently, by integrating (23a, b) and (24a-c) in relation with variables  $\overline{\alpha}_r$  and  $\overline{\beta}_r$  and under restrictions

$$\begin{aligned} l_1 &\approx \delta\pi b, \\ l_2 &\approx \nu\pi a, \\ \nu, \delta &= 1, 2, \dots \end{aligned} \quad (25a-c)$$

This is shown in Figs. 4a, b (for different values of the parameters  $\nu$ ,  $\delta = 1, 2, \dots$  and  $r$ ).

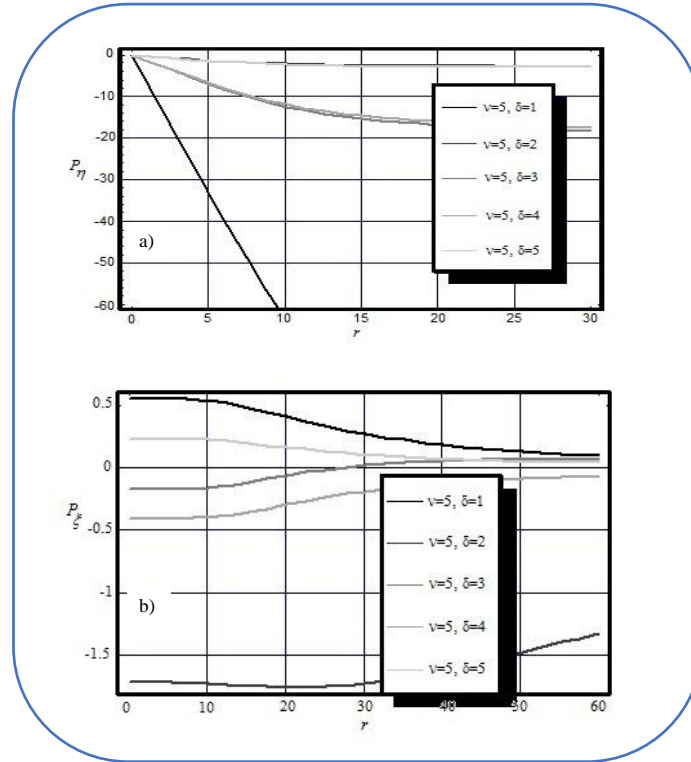


Fig. 4 – Plot of pressure  $p_\eta$  on the planes, versus parameter  $r$  for  $v = 5$ ,  $\delta = 1, \dots, 5$  (a); Plot of pressure  $p_\xi$  versus parameter  $r$  for  $v = 5$ ,  $\delta = 1, \dots, 5$  (b).

We must highlight the following conclusions: a) pressure  $p_\eta$  on the planes, given by (26a) stabilized for great  $r$  values, is always negative, hence an attractive force (Fig. 4a); b) besides pressure  $p_\eta$  acting on the planes, another pressure must manifest,  $p_\xi$  (Fig. 4b), acting along the  $O\xi$  axis and given by (26b). Thus we notice that this pressure becomes null for great  $r$  values, and has a minimum for some values of the parameters  $m$ ,  $n$ ; c) if the planes were in the  $\eta O \zeta$  plane, the self-constraints being along the  $O\xi$  axis, vortices streets would form along this axis and the result in (23a, b) with (24a-c) would have been applied, *i.e.* the cases i) or ii) are identical, nonetheless they depend on the selected geometry; d) the pressures  $p_\xi(\beta_1)$  and  $p_\xi(\beta'_1)$  generate tensions of internal friction, while  $p_\eta(\alpha_1)$  and  $p_\eta(\alpha'_1)$  generate compression tensions in the attractive case and stretching tensions in the repulsive case; e) if one tries to compute the order of magnitude of the force between the planes, and replaces in (23b) or (25b):  $\Gamma = h/2\pi m = 1.054 \cdot 10^{-34} \text{ Js}/10^{-27} \text{ kg} \approx 10^{-7} \text{ m}^2/\text{s}$ ,

$\rho \approx 10^3 \text{ kg/m}^3$  ( $a, b \approx 10^{-6} \text{ m}$  (specific values for the boundary layer) and  $l_1, l_2 \approx 5a, 5b$  (the distances between the planes) a value for  $p_\xi(\overline{\beta_1})$  can be obtained,  $p_\xi(\overline{\beta_1}) \approx 10 \text{ N/m}^2$ , *i.e.* of the order of viscous dissipation tension (Lifshičtīs and Landau, 1987). A similar calculus can be made for Cooper-type pairs in the case of type I superconductors (Poole *et al.*, 1995).

#### 4. Conclusions

The main conclusions of the present paper are presented in the following:

i) A short description of the differentiable-non-differentiable scale transition dynamics is made (implying momentum and states density conservation laws).

ii) Applying this specific formalism, it can be shown that, in the case of a two-dimensional non-differentiable and non-coherent fluid, with its entities assimilated to vortex-type objects, the coherence induces vortices streets.

iii) Furthermore, if the fluid bears self-constraints from the two planes, then on their normal axis a coherent structure of vortex street type appears. In this case, the interaction forces (being either attractive or repulsive) between the two planes can be assessed. Then, a Cazimir-type effect (Wilson *et al.*, 2011) at small scales and a Tiffit-type effect (Tiffit, 1982) at large scales can manifest. At nanoscales, such an effect could explain the fractional or integer quantum Hall effect (Rao and Sood, 2013) in graphenes.

iv) This theoretical model can be applied to infra and extra galactic scales, for which the vortex constant is related to a gravitational-type Planck constant (Agnese and Festa, 1997).

v) Moreover, in our opinion, by being able to understand the rules which determine the structure coherence of complex fluids, one can find the most viable solution for explaining the specific individual variations in the evolution and prognosis of different types of cardiovascular diseases (Mäkikallio *et al.*, 2001).

We note that the same model can also be applied, because of its theoretical implications, in engineering and materials science, in various domains, such as the ones described in (Agape *et al.*, 2016; Agape *et al.*, 2017; Gaiginschi and Agape, 2016; Gaiginschi *et al.*, 2011; Gaiginschi *et al.*, 2014a; Gaiginschi *et al.*, 2014b; Gaiginschi *et al.*, 2017; Vornicu *et al.*, 2017).

## REFERENCES

- Agape I., Gaiginschi L., Gaiginschi R., Baltagiu D., *Upon a Simple Method for Generating Transversal Profile of the Volumic Blower Rotor Used in Supercharging ICE*, *Ingineria Automobilului*, **38**, 22-25 (2016).
- Agape I., Gaiginschi L., Ianuș G., Cimpoeșu N., *The Analysis of an Internal Combustion Engine Breakdown - Case Study*, *IOP Conference Series: Materials Science and Engineering*, **209**, 1, 012077 (2017).
- Agnese A.G., Festa R., *Clues to Discretization on the Cosmic Scale*, *Phys Lett A*, Vol. 227, 165-171 (1997).
- Agop M., Casian-Botez I., *Theoretical Approach of Differentiable-Non-Differentiable Scale Transition in Nanostructures*, *Journal of Computational and Theoretical Nanoscience*, **12**, 1-12 (2015).
- Aronstein D.L., Stround Jr.C.R., *Fractional Wave-Function Revivals in the Infinite Square Well*, *Phys. Rev. A*, **5**, 1050-2947 (1997).
- Armitage J.V., Eberlein W.F., *Elliptic functions*, Cambridge University Press, Cambridge, 2006.
- Casian-Botez I., Agop M., *Order-Disorder Transition in Nanostructures via Non-Differentiability*, *Journal of Computational and Theoretical Nanoscience*, **12**, 1-10 (2015).
- Cristescu C.P., *Dinamici Neliniare si Haos, Fundamente Teoretice si Aplicatii*, Ed. Academiei Romane, București, 2008.
- Gaiginschi L., Agape I., *Upon an Issue of Correlation Between the Running Speed of Vehicles and Traffic Capacity of a Road Section*, *IOP Conference Series: Materials Science and Engineering*, **147**, 1, 012118 doi:10.1088/1757-899X/147/1/012118 (2016).
- Gaiginschi L., Gaiginschi R., Agape I., Hantoiu V., *Researches Regarding Impact Energy Dissipation by Breaking for Front – Rear Collisions*, *Ingineria Automobilului*, **18**, 20-23 (2011).
- Gaiginschi L., Agape I., Sachelarie A., Girbaci M.A., *Virtual High Speed Diesel Engine – A Simulated Experiment. Part I: Combustion Dynamics*, *Applied Mechanics and Materials*, **659**, 189-194 (2014a).
- Gaiginschi L., Agape I., Sachelarie A., Girbaci M.-A., *Virtual High Speed Diesel Engine – A Simulated Experiment. Part II: The Influence of Polytropic Exponent upon Combustion Product Formation*, *Applied Mechanics and Materials*, **659**, 195-200 (2014b).
- Gaiginschi L., Agape I., Talif S., *Upon the Reconstruction of Accidents Triggered by Tire Explosion. Analytical Model and Case Study*, *IOP Conf. Series: Materials Science and Engineering*, **252**, 012016 doi:10.1088/1757-899X/252/1/012016 (2017).
- Gottlieb I., Agop M., Jarcau M., *El Naschie's Cantorian Space-Time and General Relativity by Means of Barbilian's Group. A Cantorian Fractal Axiomatic Model of Space-Time*, *Chaos Solitons & Fractals*, **19**, 4, 705-730 (2004).
- Lifshičițis E.M., Landau L.D., *Fluid Mechanics*, Pergamon Press, Oxford, 1987.
- Kawahara G., Kida S., *Anatomy of Turbulence - Flow Structure and its Function*, Kyoto University, Research Institute for Mathematical Sciences, Kyoto, 2004.

- Kauffmann G., White S.D.M., Guiderdoni B., *The Formation and Evolution of Galaxies within Merging Dark Matter Haloes*, Mon. Not. R. Astron. Soc., **264**, 201-218 (1993).
- Mäkikallio T.H., Huikuri H.V., Mäkikallio A., Sourander L.B., Mitrani R.D., Castellanos A., Myerburg R.J., *Prediction of Sudden Cardiac Death by Fractal Analysis of Heart Rate Variability in Elderly Subjects*, J Am Coll Cardiol., **37**, 5, 1395-402 (2001).
- Mandelbrot B.B., *The Fractal Geometry of Nature* (Updated and Augm. Ed.), W.H. Freeman, New York, 1983.
- Munceanu G.V., Păun V.-P., Casian-Botez I., Agop M., *The Microscopic-Macroscopic Scale Transformation Through a Chaos Scenario in the Fractal Space-Time Theory*, International Journal of Bifurcation and Chaos, **21**, 2, 603-618 (2011).
- Nottale L., *Fractal Space-Time and Microphysics: Towards a Theory of Scale Relativity*, World Scientific, Singapore, 1993.
- Nottale L., *Scale Relativity and Fractal Space-Time – A New Approach to Unifying Relativity and Quantum Mechanics*, Imperial College Press, London, 2011.
- Poole C.P., Farach H.A., Creswick R.J., *Superconductivity*, Academic Press, San Diego, 1995.
- Rao C.N.R., Sood A.K., *Graphene: Synthesis, Properties, and Phenomena*, John Wiley & Sons, New York, 2013.
- Reguera D., Bonilla, L.L., Rubi, J.M., *Coherent Structures in Complex Systems: Selected Papers of the XVII Sitges Conference on Statistical Mechanics Held at Sitges, Barcelona, Spain, 5–9 June 2000*, Springer, Berlin, 2008.
- Schive H.-Y., Chiueh T., Broadhurst T., *Cosmic Structure as the Quantum Interference of a Coherent Dark Wave*, Nature Physics, **10**, 496-499 (2014).
- Tesloianu N.D., *PAD and COPD in Smokers – Physic-Mathematical and Physio-Pathological Interrelations*, Ars Longa, Iași, 2015.
- Tesloianu N.D., Ghizdovăț V., Agop M., *Flow Dynamics via Non-Differentiability and Cardiovascular Disease. A Proposal for an Interdisciplinary Approach Between Non-Differentiable Physics and Cardiovascular Morphopatology*, Scholars' Press, Saarbrücken, 2015.
- Tiftt W.G., *Quantum Effects in the Redshift Intervals for Double Galaxies*, Astrophys. J., **257**:442 (1982).
- Timofte A., Casian-Botez I., Scurtu D., Agop M., *System Dynamics Control Through the Fractal Potential*, Acta Physica Polonica A, **119**, 3, 304-311 (2011).
- Toda M., *Theory of Nonlinear Lattices*, 2nd Enl. Ed., Springer, Berlin, 1989.
- Vornicu V., Ulian T., Rakosi E., Manolache Gh., Gaiginschi L., *Theoretical Model for Determination of the Spark Ignition Engine Thermo-Gasodynamic Parameters on Various Functional Conditions*, IOP Conference Series: Materials Science and Engineering, **252**, 1, 012073 doi:10.1088/1757-899X/252/1/012073 (2017).
- Wilson C.M., Johansson G., Pourkabirian A., Simoen M., Johansson J.R., Duty T., Nori F., Delsing P., *Observation of the Dynamical Casimir Effect in a Superconducting Circuit*, Nature, **479**, 376-379 (2011).

## COERENȚA ÎN STRUCTURILE FRACTALE

(Rezumat)

Prin aplicarea Teoriei Relativității de Scară într-o dimensiune fractală de constantă arbitrară, se arată că, pentru un fluid necoerent nediferențibil bidimensional, ale cărui entități pot fi asimilate cu obiecte de tip vortex, mecanismul de coerență induce străzi de vortexuri. Într-un caz particular, dacă fluidul prezintă limitări date de cele două plane, forța de interacțiune (fie de tip atractiv, fie de tip repulsiv) dintre cele două plane poate fi determinată. Atunci, se pot observa efecte de tip Cazimir la scări mici și efecte de tip Tiffit la scări mari (extragalactice). La nanoscară, acestea pot explica efectul Hall fracționat sau integrat în grafene.

## ON A “HIDDEN” SYMMETRY OF THE MAXWELL’S EQUATIONS

BY

IRINEL CASIAN BOTEZ<sup>1,\*</sup> and MARICEL AGOP<sup>2,3</sup>

“Gheorghe Asachi” Technical University of Iași, Romania,

<sup>1</sup>Faculty of Electronics, Telecommunication and Information Technology

<sup>2</sup>Department of Physics

<sup>3</sup>Academy of Romanian Scientists, București, Romania

Received: February 26, 2018

Accepted for publication: April 11, 2018

**Abstract.** It is show that the Maxwell’s equations have a “hidden” symmetry on the form of the Barbilian’s group. Some properties and implications of this group is also analyzed.

**Keywords:** Maxwell’s equations; Barbilian’s group; Jaine’s probability.

### 1. Introduction

Let us consider the Maxwell’s equations in simple media (non-dispersive, linear and isotropic) without sources (Harrington, 2001):

$$\begin{aligned}\nabla \times \mathbf{E} &= -\mu \frac{\partial \mathbf{H}}{\partial t} \\ \nabla \times \mathbf{H} &= \varepsilon \frac{\partial \mathbf{E}}{\partial t} + \sigma \mathbf{E} \\ \nabla \cdot \mathbf{H} &= 0 \\ \nabla \cdot \mathbf{E} &= 0\end{aligned}\tag{1}$$

---

\*Corresponding author; *e-mail*: irinel\_casian@yahoo.com

Using vectorial calculus, we can transform these equations in two wave equations, one in electric field,  $\mathbf{E}$ , and the other in magnetic field,  $\mathbf{H}$ :

$$\nabla^2 \mathbf{E} = \varepsilon\mu \frac{\partial^2 \mathbf{E}}{\partial t^2} + \mu\sigma \frac{\partial \mathbf{E}}{\partial t} \quad (2)$$

$$\nabla^2 \mathbf{H} = \varepsilon\mu \frac{\partial^2 \mathbf{H}}{\partial t^2} + \mu\sigma \frac{\partial \mathbf{H}}{\partial t} \quad (3)$$

We only continue with the equation in electric field, since the equation in magnetic field has the same form.

In Cartesian coordinate systems, the vectorial Eq. (2) is equivalent with 3 similar scalar equations:

$$\nabla^2 E_i = \varepsilon\mu \frac{\partial^2 E_i}{\partial t^2} + \mu\sigma \frac{\partial E_i}{\partial t}, \quad i = x, y, z \quad (4)$$

For this equation a “hidden” symmetry in the form of Barbilian’s group is given.

## 2. Mathematical Model

Every component is a scalar function of space and time. Following the method of variables separation, we consider:

$$E_i(x, y, z, t) = g_i(x, y, z)T(t), \quad i = x, y, z \quad (5)$$

So, the Eq. (4) become:

$$\nabla^2 g_i - \lambda_i g_i = 0 \quad (6)$$

$$\frac{d^2 T}{dt^2} + \frac{\sigma}{\varepsilon} \frac{dT}{dt} - \frac{\lambda_i}{\mu} T = 0 \quad (7)$$

Now, we restrain the problem to one-dimensional (1D) case, *i.e.* that the electric field has component only in x-direction. In this situation,  $g_i(x, y, z) = \theta(x)$  and the Eqs. (6) and (7) become:

$$\frac{d^2 \theta}{dx^2} + k_0^2 \theta(x) = 0 \quad (8)$$

$$\frac{d^2T}{dt^2} + \frac{\sigma}{\varepsilon} \frac{dT}{dt} + \frac{k_0^2}{\mu} T = 0 \quad (9)$$

where

$$-\lambda_i = k_0^2$$

The most general solution of the Eq. (8) can be written in the form:

$$\theta(x) = h e^{i(k_0x+\varphi)} + \bar{h} e^{-i(k_0x+\varphi)} \quad (10)$$

with  $h$  a complex amplitude,  $\bar{h}$  its complex conjugate and  $\varphi$  a phase.

This solution describes a complex system structural units (electrical field – material structures) of the same “characteristic”  $k_0$ , in which the structural unit is identified by means of the parameters  $h, \bar{h}$  and  $k = e^{i\varphi}$ . Now, a question arises. Which is the relation among the structural units of the complex system having the same  $k_0$ ? The mathematical answer to this question can be obtained if we admit that all we intend here is to find a way to switch from a triplet of numbers - the initial conditions - of a structural unit, to the same triplet of another structural unit having the same  $k_0$ .

This passage implies a “hidden symmetry” which is made explicit in the form of a continuous group with three parameters, group that is simple transitive and which can be constructed using a certain definition of  $k_0$ .

We start from the idea that the ratio between two fundamental solutions of Eq. (8) is a solution of Schwartz’s nonlinear equation (Mihăileanu, 1972):

$$\{\tau_0(x), x\} = 2k_0^2, \quad \tau_0(x) = e^{-2ik_0x} \quad (11)$$

where the curly brackets define Schwartz’s derivative of  $\tau_0$  with respect to  $x$ ,

$$\{\tau_0(x), x\} = \partial_x \left( \frac{\partial_{xx} \tau_0}{\partial_x \tau_0} \right) - \frac{1}{2} \left( \frac{\partial_{xx} \tau_0}{\partial_x \tau_0} \right)^2 \quad (12)$$

This equation proves to be a veritable definition of  $k_0$ , as a general characteristic of a complex system of structural units which can be swept through a continuous group with three parameters - the homographic group.

Indeed, Eq. (11) is invariant with respect to the dependent variable change:

$$\tau(x) = \frac{a\tau_0(x) + b}{c\tau_0(x) + d}, \quad a, b, c, d \in \mathbb{R} \quad (13)$$

and this statement can be directly verified.

In this way,  $\tau(x)$  characterizes another structural unit of the same  $k_0$ , which allows us to state that, starting from a standard structural unit, we can sweep the entire complex system of structural units having the same  $k_0$ , when we are not conditioning (we leave it free) the three ratios  $a : b : c : d$  in Eq. (13).

We can make even more accurate the correspondence between a homographic transformation and a structural unit of the complex system, by associating to every structural unit of the complex system, a “personal”  $\tau(x)$  by the relation:

$$\tau_1(x) = \frac{h + \bar{h}k\tau_0(x)}{1 + k\tau_0(x)}, \quad k = e^{-2i\phi} \quad (14)$$

Let us observe that  $\tau_0$  and  $\tau_1$  can be used freely one in place of another and this leads us to the following transformation group for the initial conditions:

$$h \leftrightarrow \frac{ah+b}{ch+d}, \bar{h} \leftrightarrow \frac{a\bar{h}+b}{c\bar{h}+d}, k \leftrightarrow \frac{c\bar{h}+d}{ch+d}k \quad (15)$$

This group is simple transitive: to a given set of values  $(a/c, b/c, d/c)$  will correspond a single transformation and only one of the group.

The group (15) works as a group of “synchronization” among the various structural units of the complex system, process to which the amplitudes and phases of each of them obviously participate, in the sense that they are correlated, too. More precisely, by means of (15), the phase of  $k$  is only moved with a quantity depending on the amplitude of the structural unit of complex system at the transition among various structural units of the complex system. But not only that, the amplitude of the structural unit of the complex system is also affected homographically.

The usual “synchronization” manifested through the delay of the amplitudes and phases of the structural units of the complex system must represent here only a totally particular case.

**Theorem 1:** *In the “field variables” space of the synchronization group one can a priori build a probabilistic theory based on its elementary measure, as an elementary probability. Then the invariant function of the synchronization group becomes the repartition density of an elementary probability.*

The proof of these statements is based on the differential and integral properties of the homographic group. Thus, considering a specific parametrization of the group (15), the infinitesimal generators (Mercheș and Agop, 2015):

$$\hat{B}_1 = \frac{\partial}{\partial h} + \frac{\partial}{\partial \bar{h}}, \hat{B}_2 = h \frac{\partial}{\partial h} + \bar{h} \frac{\partial}{\partial \bar{h}}, \hat{B}_3 = h^2 \frac{\partial}{\partial h} + \bar{h}^2 \frac{\partial}{\partial \bar{h}} + (h - \bar{h})k \frac{\partial}{\partial k} \quad (16)$$

satisfy the commutation relations:

$$[\hat{B}_1, \hat{B}_2] = \hat{B}_1, [\hat{B}_2, \hat{B}_3] = \hat{B}_3, [\hat{B}_3, \hat{B}_1] = -2\hat{B}_2 \quad (17)$$

The structure of the group (15) is given by Eq. (17) so that the only non-zero structure constants should be:

$$C_{12}^1 = C_{23}^3 = -1, C_{31}^2 = -2 \quad (18)$$

Therefore, the invariant quadratic form is given by the “quadratic” tensor of the group (15):

$$C_{\alpha\beta} = C_{\alpha\nu}^{\mu} C_{\beta\mu}^{\nu} \quad (19)$$

where summation over repeated indices is understood. Using (18) and (19), the tensor  $C_{\alpha\beta}$  writes:

$$C_{\alpha\beta} = \begin{pmatrix} 0 & 0 & -4 \\ 0 & 2 & 0 \\ -4 & 0 & 0 \end{pmatrix} \quad (20)$$

meaning that the invariant metric of the group (15) has the form:

$$\frac{ds^2}{g^2} = \omega_0^2 - 4\omega_1\omega_2 \quad (21)$$

with  $g$  an arbitrary factor and  $\omega_\alpha$ ,  $\alpha = 1, 2, 3$  three differential 1-forms (Flanders, 1989), absolutely invariant through the group (15). Barbilian takes

these 1-forms as being given by the relations (Barbilian, 1937; Mercheş and Agop, 2015):

$$\omega_0 = -i \left( \frac{dk}{k} - \frac{dh + d\bar{h}}{h - \bar{h}} \right), \omega_1 = \frac{dh}{(h - \bar{h})k}, \omega_2 = \frac{-kd\bar{h}}{(h - \bar{h})} \quad (22)$$

so that the metric (21) becomes

$$\frac{ds^2}{g^2} = - \left( \frac{dk}{k} - \frac{dh + d\bar{h}}{h - \bar{h}} \right)^2 + 4 \frac{dh d\bar{h}}{(h - \bar{h})^2} \quad (23)$$

It is worthwhile to mention a property connected to the integral geometry: the group (15) is measurable. Indeed, it is simply transitive and, since its structure vector:

$$C_\alpha = C_{\nu\alpha}^\nu \quad (24)$$

is identically null, as it can be seen from (18), this means that it possess the invariant function:

$$F(h, \bar{h}, k) = - \frac{1}{(h - \bar{h})^2 k} \quad (25)$$

which is the inverse of the modulus of determinant of a linear system obtained on the basis of infinitesimal transformations of the group (15).

As a result, in the space of the field variables  $(h, \bar{h}, k)$  one can *a priori* construct a probabilistic theory in the sense of Jaynes (on the circumstances left unspecified in an experiment), based on the elementary measure of the group (15):

$$dP(h, \bar{h}, k) = - \frac{dh \wedge d\bar{h} \wedge dk}{(h - \bar{h})^2 k} \quad (26)$$

as elementary probability, where  $\wedge$  denotes the external product of the 1-forms. In such context, the invariant function of the group (15), *i.e.* relation (25), becomes the repartition density of the elementary probability (26). An attitude toward Quantum Mechanics which is suitable for Quantum Gravity in general, and for its application to cosmology in particular, is not so easy to find. A

philosophically realistic attitude toward Quantum Mechanics would seem to be more effective than one based on operators which must find their physical meaning in terms of measurements. Where Quantum Theory differs from Classical Mechanics (in this view) is in its dynamics, which of course is stochastic rather than deterministic. As such, the theory functions by furnishing probabilities for sets of histories. What ordinarily makes it difficult to regard Quantum Mechanics as in essence a modified form of probability theory, is the peculiar fact that it works with complex amplitudes rather than directly with probabilities, the former being more like square roots of the latter. In this context the above mentioned whole arsenal of Quantum Mechanics can be extended to fractal manifolds by means of a Jaynes type procedure (Jaynes, 1973).

The above results can be re-written in real terms based on the transformation:

$$(h, \bar{h}, k) \rightarrow (u, v, \phi) \quad (27)$$

which can be made explicit through the relations

$$h = u + iv, \bar{h} = u - iv, k = e^{i\phi} \quad (28)$$

Thus, both the operators (16) and the 1-forms (22) have the expressions:

$$\hat{M}_1 = \frac{\partial}{\partial u}, \hat{M}_2 = u \frac{\partial}{\partial u} + v \frac{\partial}{\partial v}, \hat{M}_3 = (u^2 - v^2) \frac{\partial}{\partial u} + 2uv \frac{\partial}{\partial v} + 2v \frac{\partial}{\partial \phi} \quad (29)$$

Respectively

$$\begin{aligned} \Omega^1 \equiv \omega^0 &= d\phi + \frac{du}{v}, \Omega^2 = \omega^1 = \cos \phi \frac{du}{v} + \sin \phi \frac{dv}{v}, \Omega^3 = \\ &= \omega^2 = -\sin \phi \frac{du}{v} + \cos \phi \frac{dv}{v} \end{aligned} \quad (30)$$

while the 2-form (23) reduces to the two-dimensional Lorentz metric

$$-(\Omega^1)^2 + (\Omega^2)^2 + (\Omega^3)^2 = -\left(d\phi + \frac{du}{v}\right)^2 + \frac{du^2 + dv^2}{v^2} \quad (31)$$

**Theorem 2:** *The existence of a transport of directions in the Levi-Civita sense in the field variables space substitutes the homographic group with that of spin as a synchronization group.*

Let us focus on the metric (23) or (31). It is reduced to the metric of Lobachewski's plane in Poincare's representation:

$$\frac{ds^2}{g^2} = 4 \frac{dh d\bar{h}}{(h - \bar{h})^2} \quad (32)$$

for the condition  $\omega_0 = 0$ , *i.e.*, in real terms (28)

$$d\phi = -\frac{du}{v} \quad (33)$$

Since by this restriction the metric (31) in the variables (28) reduces to Lobachewski's one in Beltrami's representation:

$$\frac{ds^2}{g^2} = -\frac{du^2 + dv^2}{v^2} \quad (34)$$

the condition (33) defines a parallel transport of vectors in the sense of Levi-Civita (the definition of the parallelism angle in the Lobachewski plane, that is, the form of connection (Agop *et al.*, 2015; Mercheş and Agop, 2015): the application point of the vector moves on the geodesic, the vector always making a constant angle with the tangent to the geodesic in the current point. Indeed, taking advantage of the fact that the metric of the plane is conformal Euclidean, we can calculate the angle between the initial vector and the vector transported through parallelism, as the integral of the equation (Agop *et al.*, 2015; Mercheş and Agop, 2015).

$$d\phi = \frac{1}{2} \left[ \frac{\partial}{\partial v} (\ln F) du - \frac{\partial}{\partial u} (\ln F) dv \right], F(u, v) = \frac{1}{v^2} \quad (35)$$

along the transport curve.

Since  $F(u, v)$  represents the conformal factor of the given metric, introducing it in (35), we find (33).

The "ensemble" of the initial conditions of the structural units of the complex system corresponding to the same  $k_0$  can be organized as a geometry of the hyperbolic plane. More precisely, these structural units of the complex system correspond to a situation where their initial conditions can be chosen from among points of a hyperbolic plane.

The existence of the parallel transport in the sense of Levi-Civita (33) implies either the substitution of the operators (16) with the operators:

$$\hat{B}'_1 = \frac{\partial}{\partial h} + \frac{\partial}{\partial \bar{h}}, \hat{B}'_2 = h \frac{\partial}{\partial h} + \bar{h} \frac{\partial}{\partial \bar{h}}, \hat{B}'_3 = h^2 \frac{\partial}{\partial h} + \bar{h}^2 \frac{\partial}{\partial \bar{h}} \quad (36)$$

in the case of the representation in complex variables, or the substitution of the operators (29) with the operators:

$$\hat{M}'_1 = \frac{\partial}{\partial u}, \hat{M}'_2 = u \frac{\partial}{\partial u} + v \frac{\partial}{\partial v}, \hat{M}'_3 = (u^2 - v^2) \frac{\partial}{\partial u} + 2uv \frac{\partial}{\partial v} \quad (37)$$

in the case of the representation in real variables.

**Theorem 3:** *Through the correlation phase-amplitude given by the relation (33), the operators (37) reduce to the spin operators in the null vectors space*

$$\hat{S}_1 = \cos \psi v \frac{\partial}{\partial v} - \sin \psi \frac{\partial}{\partial \psi}, \hat{S}_2 = \sin \psi v \frac{\partial}{\partial v} + \cos \psi \frac{\partial}{\partial \psi}, \hat{S}_3 = i \frac{\partial}{\partial \psi} \quad (38)$$

Precisely, we discuss about the compactification of the angular momentum in the null vectors space in the form of the spin.

These operators multiplied with the factor  $\lambda(dt)^{(2/D_F)-1}$ , are identical, with the fractal angular momentum operators in the representations:

$$x = v \sin \psi, y = -v \cos \psi, z = iv \quad (39)$$

One can directly verify that, abstraction by a constant factor, the operators (38) are just the fractal spin operators satisfying the same commutation relations as Pauli matrix  $\sigma_i$  ( $i = 1, 2, 3$ ). They can be interpreted as fractal angular momentum operators in the fractal space of null radius

$$x^2 + y^2 + z^2 = 0 \quad (40)$$

The corresponding variables ( $v, \psi$ ) are not concrete variables but just only internal freedom degrees. Moreover, the differential and integral geometry of this group imply the “explanation of the circumstances left unspecified in an experiment” in the Jaynes probabilistic theory, while the

compactification of the angular momentum in the null vectors space through the definition of a parallel transport on directions in the Levi-Civita sense in a hyperbolic space implies the spin.

### 3. Conclusions

It is shown that the Maxwell's equations have a "hidden" symmetry in the form of Barbilian's group. In such conjecture, some implications and properties of this group are given.

### REFERENCES

- Agop M., Gavriluț A. *et al.*, *Implications of Onicescu's Informational Energy in Some Fundamental Physical Models*, International Journal of Modern Physics B 29(1550045) (2015).
- Barbilian D., *Die von einer Quantik induzierte Riemannsche Metrik (in German)*, Comptes Rendus de l'Academie Roumaine des Sciences, **2**, 198 (1937).
- Flanders H., *Differential Forms with Applications to the Physical Science*, New York, Dover Publication (1989).
- Harrington R.F., *Time-Harmonic Electromagnetic Fields*, New York, IEEE Press (2001).
- Jaynes E.T., *The Well Posed Problem*, Foundations of Physics, **3**, 477-493 (1973).
- Mercheș I., Agop M., *Differentiability and Fractality in Dynamics of Physical Systems*, World Scientific (2015).
- Mihăileanu M., *Differential, Projective and Analytical Geometry (in Romanian)*. Bucharest, Didactic and Pedagogical Publishing House (1972).

### ASUPRA UNEI SIMETRII „ASCUNSE” A ECUAȚIILOR LUI MAXWELL

(Rezumat)

Se arată că ecuațiile câmpului electromagnetic prezintă o simetrie „ascunsă” ce se poate explicita sub forma grupului de invariantă Barbilian. Într-o asemenea conjunctură, câteva proprietăți și implicații ale acestui grup sunt de asemenea date.